# LANGMUIR

pubs.acs.org/Langmuir Article

# Dynamic Drop Penetration of Horizontally Oriented Fiber Arrays

Gene Patrick S. Rible, Michael A. Spinazzola, III, Robert E. Jones, III, Rachel U. Constantin, Wei Wang, and Andrew K. Dickerson\*



Cite This: https://doi.org/10.1021/acs.langmuir.4c00371



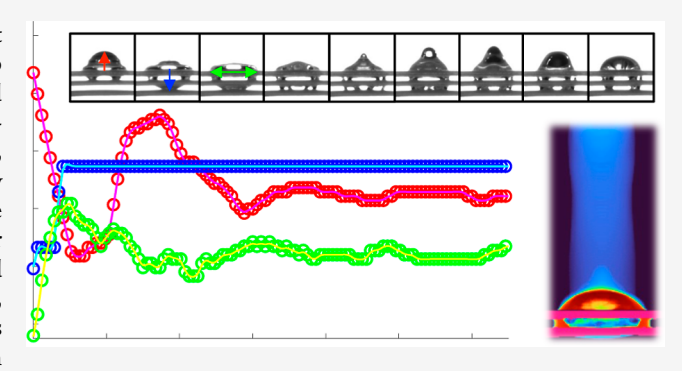
**ACCESS** I

III Metrics & More

Article Recommendations

Supporting Information

**ABSTRACT:** In this experimental study, we combine drop impact into porous media and onto a single fiber to study drop impact into fiber arrays inspired by mammalian fur coats. In our 3D-printed arrays, we vary the packing density, fiber alignment, strand cross-section, and wettability. Drops impact fibers fixed at both ends, penetrating over short periods of time by momentum and laterally spreading throughout the array. Using image analysis, we measure penetration depth and wetted width into the array. Impact Weber number and intrinsic porosity define penetration, retraction, and rebound regimes. On average, at an impact Weber number of ≈80, staggered fibers reduce penetration by 24% in hydrophilic fibers and 34% in hydrophobic fibers, and the penetration reduction



percentage is expected to increase with increasing Weber number. Our results indicate that as density grows toward the density of mammalian pelts, penetration will reach a maximum value independent of drop impact velocity, thereby providing an effective rain barrier. Hydrophilicity at the densities we test,  $50-150 \text{ strands/cm}^2$ , aids fiber array resistance to dynamic penetration by impacting drops through the promotion of lateral drop spreading and inhibition of drop fragmentation. Conversely, hydrophobic fibers best resist low-speed wicking. The fraction of a drop that infiltrates hydrophilic and hydrophobic fibers is nearly identical for a fixed Weber number because lateral spreading restricts the penetration depth into hydrophilic fibers but does not restrict mass infiltration. Above a critical Weber number, the entire drop mass penetrates fiber arrays regardless of strand wettability.

# **■ INTRODUCTION**

The state of being wet in a cold environment is dangerous for most mammals. Humans have developed raincoats and umbrellas to protect our nearly hairless skin, but evolution has bequeathed our furry counterparts with arrays of hairs for the same task. Fur is a wonderfully multipurpose and multiscale structure<sup>1-4</sup> that serves to keep mammals warm and dry,<sup>4-7</sup> provide mechanical protection,<sup>8</sup> and repel contaminants. 9,10 Fur thus permits a mammal to regulate its body temperature 11,12 and avoid undesired mass that would otherwise hinder locomotion.<sup>13</sup> An understanding of how the multiscale properties of fur work in concert to reject biofilms and other inorganic foulers is just now beginning to be understood, 10 but the ability of fur to repel high-speed drops across its morphological perturbations remains understudied. Simply, the impact of drops onto fibrous arrays mimicking those of mammalian fur appears absent in scientific literature. In this study, we investigate the impact and penetration of falling drops into simplified fiber arrays inspired by mammalian fur but produced in our laboratory such that we can fine-tune fiber properties. Thus, we strive to uncover the mechanics of drop impact onto such media and shed further light on the multifunctional wonder that is natural fur.

Mammal fur has a vast diversity in length, density, coarseness, and curl. The long hair of an orangutan stands in

contrast to the hydrophobic, lanolin-covered <sup>14</sup> curls of a Scottish Dunface sheep. The most densely packed pelts are found on semiaquatic mammals such as sea otters <sup>13</sup> that have underfurs topping  $O(10^5)$  strands/cm<sup>2</sup>. Otter fur also has the ability to interlock strands to promote the capture and retention of air while submerged. <sup>15</sup> Terrestrial mammals in hot climates have much sparser pelts, like that of the bushpig <sup>13</sup> with O(10) strands/cm<sup>2</sup>. No matter the wettability, density, length, or coarseness, most furs are simply a porous medium consisting of fibers arranged locally parallel to one another. Some furs lie flat, whereas others stand erect. We simplify the fur system for experimentation by considering only horizontally oriented artificial samples, which are 3D-printed parallel fiber arrays rigidly affixed at both ends. Our fiber arrays at O(100) strands/cm<sup>2</sup> are comparable to that of the gray wolf. <sup>16</sup>

The study of drops impacting fibers has been primarily carried out with singular fibers, cantilevered and fixed. Cantilevered fibers can capture impacting drops when impact

Received: January 29, 2024 Revised: May 1, 2024 Accepted: May 1, 2024



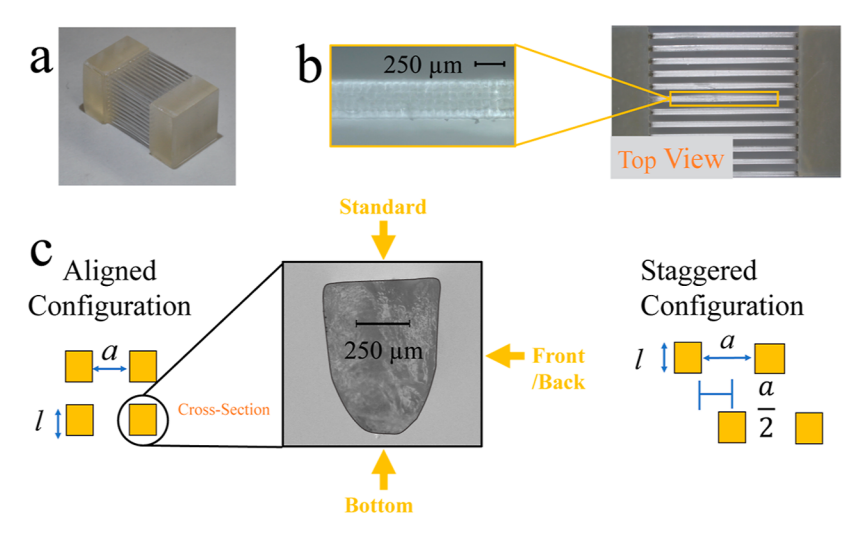


Figure 1. 3D-printed fiber array. (a) Oblique view. (b) Top view. Fixing both ends and making the fibers rigid eliminates cantilever beam dynamics.<sup>69</sup> (c) Cross-sectional view of a strand; cross-sectional asymmetry results in distinct orientations with respect to the impacting drop.

velocity is sufficiently low and fiber flexibility is sufficiently high. 17-27 Outside the capture regime, impacting drops cause cantilevered fibers to displace as the drop breaks apart, and displacement is independent of drop momentum within a drop diameter range of 2.4-3.3 mm and a Weber number range of 100-350.<sup>28</sup> Thus, fiber properties rather than drop momentum seem to dominate maximal fiber displacement following drop impact. Single fibers fixed at both ends induce drop breakup by splitting drops along the axis on impact, resulting in flat "lobes" projecting downward faster than the impacting drop.<sup>29</sup> Lobes formed by drops impacting wedged fibers are irregular, in contrast to the parabolic lobes of round fibers.<sup>29</sup> Moreover, a wedge-like shape experiences a larger corresponding impact force than its round counterpart, thereby producing a more lateral separation of the liquid lobes formed by the impacting drop.<sup>29</sup> Such disparity in generated impact force grows with larger Weber numbers.<sup>29</sup>

From the viewpoint of an impacting drop, our arrays of fixed fibers considered in this study form an anisotropic, regular porous substrate. Images of our test fibers are shown in Figure 1. Drops impacting porous media are ubiquitous in rain events<sup>30</sup> and industrial processes. Dynamics of spreading and penetration are important in inkjet and 3D-printing, cleanup processes, coating of porous substrates, irrigation, and in the manufacture of ceramic structures.<sup>31–34</sup> Droplet spreading after impingement and the spreading rate over porous surfaces are critical to the quality of inkjet printing.35-37 An understanding of the absorption of drops impacting porous materials enables the development of methods to improve cleaning techniques and mitigate toxic substance absorption.<sup>38</sup> For instance, environmental applications such as hazard assessment of accidental release of liquids onto the soil are mainly concerned with the evaporation rate of the liquid droplet, which is a function of the area of the wet spot on the surface of the porous medium that is exposed to the atmosphere, and of the penetration depth.<sup>39</sup> Liquid drops penetrating porous surfaces do so via inertia in the first moments of impact before transitioning to capillary-driven penetration over larger time scales. 30,38,40,41 The dynamic nature of impact by our drops forces the liquid near or past the extent that would be achieved by capillary wicking. 42,43 The slight amount of wicking we do observe is unaided by fiber

flexibility, as it would be in cantilevered fibers or fur. 44,45 In addition to drop momentum, the penetration depth  $d_n$  and spreading width  $\chi$  behavior of an impinging drop on a surface depend on liquid density  $\rho$ , viscosity  $\mu$ , and surface tension  $\sigma$ , as well as surface wettability, roughness, and surface motion. 46-51 On solid surfaces, drops can deposit, rebound, or splash<sup>52</sup> depending on the impact kinetics, liquid properties, surface characteristics, and temperature. 46,53 After reaching maximum spreading, the drop recedes under surface tension. 46,54 Recession time depends on several factors such as the surface shape and drop surface tension. 55,56 If the recession is sufficiently vigorous and the solid is superhydrophobic, 46 drops will jump off the surface. 47 However, during impacts with very high initial kinetic energy, drops disintegrate into secondary droplets and may splash. 47,57 Such splashing can be suppressed or enhanced by changing the orientation or curvature of the surface, changing the surface roughness,  $^{58}$  or when drops impact on a moving liquid film or surface.  $^{58-63}$  Increasing the impact velocity U induces sidesplash, and further increases in velocity lead to omnidirectional splash, whereas increasing the tangential velocity of the moving surface promotes side-splashing in the rear edge and discourages omnidirectional splash.<sup>61</sup> As the surface velocity increases, the critical impact velocity to induce splashing decreases.64

On rough porous substrates, the primary splash parameters are the impact Weber number  $We = \rho D_0 U^2/\sigma$  (where  $D_0$  is the drop size) and the characteristic roughness or grit size  $\epsilon$  of the substrate. Splashing occurs when  $We \ (\epsilon/D_0) \gtrsim 1$ . Absorption, in contrast, is governed by liquid properties as well as substrate porosity, pore size, and wettability. Once the deposited liquid drop is completely depleted from the exterior surface of the porous medium, further redistribution within the porous medium due to capillary forces is possible while evaporation occurs at the surface. See the deposite of the porous at the surface.

In this study, we allow drops of diameter  $D_0 = 2.86 \pm 0.13$  mm to impact arrays of horizontally oriented fibers, producing impact We = 1-100. Our system thus lies at the nexus of porous media and single fibers. We describe our methods of fiber production, experimentation, and image analysis in the Experimental Section. Our Results and Discussion is comprised of three subsections. Impact We and fiber array

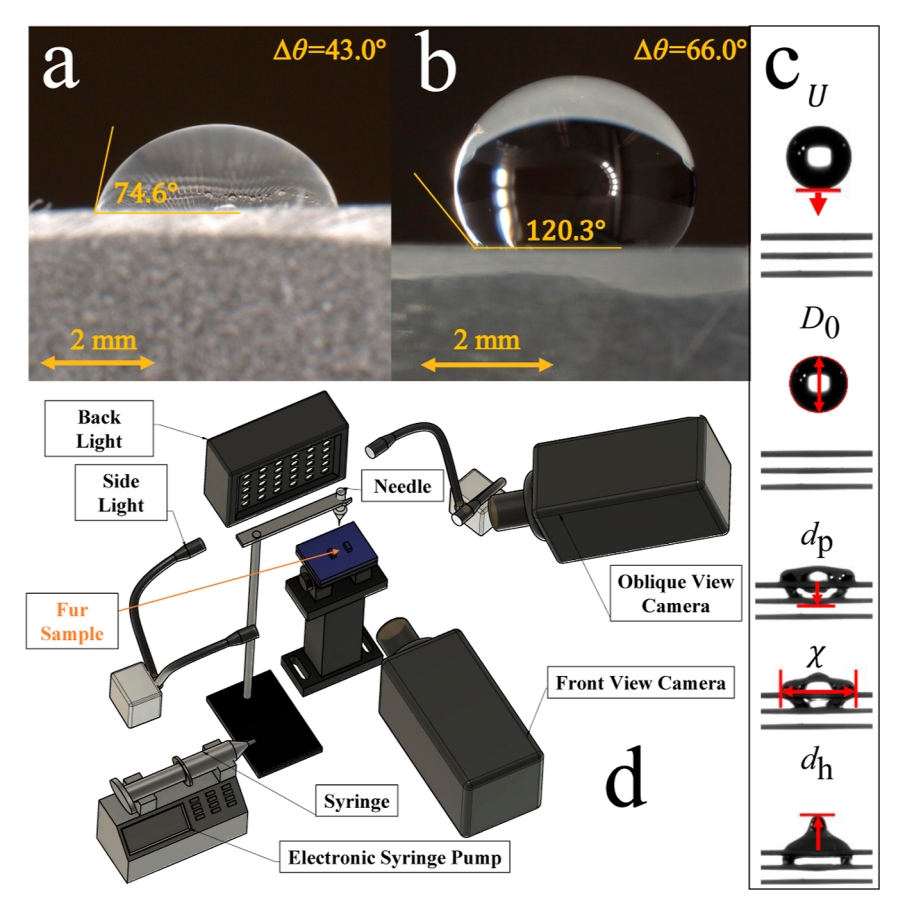


Figure 2. Contact angles of water drops on (a) hydrophilic and (b) hydrophobic fibers. (c) Measured quantities. (d) Experimental setup.

configuration produce various impact classifications that are presented in the Impact Classifications subsection. We discuss the governance of drop penetration into the arrays by consideration of energetics in the Penetration subsection. Drops spread laterally throughout the fiber arrays as they exhibit penetration, an extent that is likewise captured by an energy balance. We allow higher speed drops to impact our arrays in the Implications for Mammals and Applications subsection. We draw the work to a close in the Conclusions.

# **■ EXPERIMENTAL SECTION**

Fiber Printing and Morphology. Translucent fiber arrays are fabricated with photopolymer resin in a FlashForge Hunter DLP resin 3D printer with a layer resolution of 25  $\mu$ m and a pixel size of 62.5  $\mu$ m. According to FlashForge, the cured resin has a tensile modulus of 48 MPa and a flexural modulus of 2250 MPa. A block of resin anchors fibers at each end to ensure fiber alignment during production and experimentation, as pictured in Figure 1a. The fiber/block structure is printed such that fibers are parallel to the build plate. The fibers are 20 mm long and create a 10 mm × 10 mm array. The array size ensures that drops do not cross the array boundary over the course of impact. Printer resolution and curing dynamics limit how small and densely packed fibers can exist without clumping into a unified mass during printing. The width of our fiber cross-section  $l \approx 350 \ \mu m$ , as shown in Figure 1b. A cross-sectioned experimental fiber is pictured in Figure 1c. Fibers are designed to be square in cross-section with a dimension 1 for the sake of printing, but gravity causes the resin to flow into a wedge-like cross-section during printing in the resin bath. Therefore, the fibers have a cross-sectional width of 344  $\pm$  26  $\mu m$ (number of samples, N = 18) and a length of 394  $\pm$  50  $\mu$ m (N = 18). We note that, despite popular belief, mammalian fibers are not circular. 10,70 The unintended wedge-like shape allows us to test the

influence of cross-section orientation, standard, front/back, and bottom (Figure 1c) on drop impact outcomes.

Arrays are printed with three different permutations of interfiber spacing a to generate packing densities of approximately 50, 100, and 150 cm<sup>-2</sup>, with an average error on a of 3.8%. We produce and test two packing configurations for each packing density, one in which all fibers are aligned in a square grid (aligned) and another in which fibers in an adjacent row are shifted laterally by a/2 (staggered), as shown in Figure 1c. Fiber size and spacing, l and a, determine the intrinsic porosity of the array. The ratio of empty area to that consumed by fibers on any single row of the array is given by

$$AR = \frac{a}{l+a} \tag{1}$$

an intrinsic porosity which we call the "aspect ratio" of the array. Solid surfaces have AR = 0; single fibers AR = 1; and porous media 0 < AR < 1. Greater values of AR will intuitively result in easier penetration by an impacting drop. However, eq 1 is ignorant of drop size and thus insufficient to describe impact classification transitions.  $^{19,21,22,72,73}$  The inclusion of drop size is captured in a modified aspect ratio, AR multiplied by the ratio of fiber-plus-gap unit I + a to the drop size,  $^{74,75}$   $D_0$ 

$$AR^* = AR \frac{l+a}{D_0} = \frac{a}{D_0}, \quad \text{for} \quad l+a < D_0$$
 (2)

The ability of a drop to penetrate an array is now cursorily described by  $AR^*$ .

**Augmenting Fiber Wettability.** The cured mounting blocks at the fiber terminus (Figure 1b) provide a flat surface on which we measure the contact angles of drops. Raw prints have receding, equilibrium, and advancing contact angles of  $\theta_{\rm r}=46.3\pm9.1^{\circ}$  (number of trials N=3),  $\theta_{\rm e}=74.6\pm6.9^{\circ}$  (N=3), and  $\theta_{\rm a}=89.2\pm7.0^{\circ}$  (N=3), respectively. We make an array hydrophobic through vapor phase silanization of the samples using fluorosilane. <sup>76,77</sup> The

resulting contact angles are  $\theta_r = 62.9 \pm 8.9^{\circ}$  (N = 3),  $\theta_e = 120.3 \pm 8.1^{\circ}$  (N = 3), and  $\theta_a = 128.8 \pm 7.6^{\circ}$  (N = 3). Sessile drops are pictured on both uncoated and coated samples in Figure 2a,b.

Experimental Methodology and Principle Measurements. A schematic diagram of the experimental setup is shown in Figure 2d. For simplicity, drops of a fixed diameter  $D_0 = 2.86 \pm 0.13$  mm (N =444) are released from a needle positioned at heights h = 7, 18, 33, 120, and 1916 mm above a fiber array with impact Reynolds number Re =  $\rho U D_0 / \mu$  = 730–4300 for the first four needle heights wherein the observed flow of the drop within the fiber array is laminar; a modified Reynolds number Re\* =  $\rho Ua/\mu$  = 100–2500 based on flow in pipes 18 better characterizes the flow in our fiber arrays. For the fifth needle height discussed in Results and Discussion, the observed flow is no longer laminar with Re  $\approx$  14,500 and Re\*  $\approx$  5500. The impact Ohnesorge number  $O = \mu / \sqrt{\rho \sigma a} = 2.9 \times 10^{-3} - 5.3 \times 10^{-3}$ . Impacts are filmed with two synchronized Photron Nova S6 cameras at 3000 fps, with a resolution of approximately 25 pixels/mm. The oblique view camera is used to verify impact location but does not provide quantitative data. Between trials, samples are dried with compressed laboratory air and never contact human skin. Videos captured by the front view camera are binarized in MATLAB with no imposed dilation or erosion. From binarized video frames, we measure drop diameter  $D_0$ , temporal drop position, drop velocity U, penetration depth  $d_p$ , the drop width  $\chi$  ( $\chi = D_0$  preimpact), and the height of liquid above the array (dome height)  $d_h$ , labeled in Figure

**Dimensionless Parameters.** In the following analysis of drop impact onto fiber arrays, a number of dimensionless groups arise upon nondimensionalization of our governing equations and for the sake of convenient comparison. The principle quantities measured during and following impact are normalized by spherical drop diameter  $D_0$  to form

$$\check{d}_{\rm p} = d_{\rm p}/D_0, \qquad \check{\chi} = \chi/D_0, \quad \text{and} \quad \check{d}_{\rm h} = d_{\rm h}/D_0$$
(3)

We nondimensionalize time t by the time scale of impact such that the dimensionless inertial time  $\tau=tU/D_0$ . The moment of drop contact corresponds to  $\tau=0$ . We also denote three distinct moments during the infiltration of the fibers. The first occurs at  $\tau=T_\chi$  when the drop reaches its widest lateral extent to achieve  $\chi_{\rm m}$  and  $\check{\chi}_{\rm m}=\chi_{\rm m}/D_0$ , a wetting position it may or may not hold steadily. The second occurs at  $\tau=T_{\rm p}$  when the drop penetrates deepest into the array to achieve  $d_{\rm p,m}$  and  $\check{d}_{\rm p,m}=d_{\rm p,m}/D_0$ , a position that likewise may be held ephemerally. The third is the drop final resting position where neither wetted width nor depth measurably change in the time scale of our videos. Nomenclature of the various quantities and mathematical symbols used in the study is provided in Table 1 for convenience.

# ■ RESULTS AND DISCUSSION

**Impact Classifications.** Fiber spacing  $AR^*$ , configuration, cross-sectional profile, contact angle, and drop impact velocity U collectively govern the expression of eight identifiable impact classifications, as shown in Figure 3 and Movie S1. Impact classifications can further be subdivided into three major clusters: jet-like rebound, little jet-like rebound, and no rebound. The distinction between jet-like rebound and little jet-like rebound is made by the qualitative prominence of the jet formed as the cap of the drop rebounds upward. While small, the jet formed at  $\tau = 2.21$  ms in the sixth row of Figure 3 is the most prominent supersurface feature. The jet in the seventh row at  $\tau = 1.19$  ms is less prominent than the spreading rim. A distinction is also made between impacts where the drop breaks into fragments and those where the drop remains intact. Impact classifications without fragmentation reach steady-state in a relatively shorter time. For example, the fragmenting, penetrating drop on the sixth row of Figure 3 has an impact sequence approximately 20× longer than the

Table 1. Nomenclature

symbol	definition
ho	liquid density
$\mu$	dynamic viscosity
$D_0$	drop diameter
U	drop impact velocity
$\sigma$	surface tension
We	impact Weber number
1	cross-sectional length, refer to Figure 1
а	fiber spacing, refer to Figure 1
	fiber aspect ratio,
AR	a/(l+a)
$AR^*$	modified fiber aspect ratio, $a/D_0$
$d_{\mathrm{p}}$	drop penetration depth, refer to Figure 2
χ	drop spread width, refer to Figure 2
$d_{ m h}$	drop dome height, refer to Figure 2
$\tau = tU/D_0$	dimensionless inertial time
$T_{\chi}$	instant of maximum spread
$T_{\rm p}$	instant of maximum penetration
$k_1, k_2, k_3, k_4$	penetration coefficients, refer to eqs 22 and 23
□ <sub>□,s</sub>	steady-state value, $\square$ is a placeholder
□ <sub>□,m</sub> □	maximum value,  is a placeholder
Ŏ	normalized length value $\square/D_0$ , $\square$ is a placeholder

impact on the second row. A profile of all impact classifications, capturing the transient jet and fragmentation that arise during impact, is captured in the normalized heat maps in the leftmost column of Figure 3. The red-most colors indicate a higher incidence of drop spatial residence, whereas the blue-most colors indicate the most transience. The heat maps of Figure 3 are made from every frame of a single video and provide, in a single image, the characteristic behaviors of an impact sequence.

Impact image sequences provide an intuition that deeply penetrating drops do not have as prominent a dome as those that penetrate slightly or not at all. Therefore, we expect steady-state penetration depth  $d_{p,s}$  and steady-state dome height  $d_{h,s}$  to be negatively correlated, as explored further in the Supporting Information. Furthermore, drops that spread a greater lateral distance  $\chi_s$  are limited by volume conservation to penetrate,<sup>34</sup> as explored further in the Supporting Information. We plot  $d_{p,s}$  versus  $\chi_s$  for hydrophilic fibers and find that nonfragmenting drops behave as predicted, as shown in Figure 4a. A triangle ( $\triangle$ ,  $\triangle$ ) represents impacts where the drop forms an upward rebounding jet upon recession, whereas a circle  $(\bullet, \bigcirc)$  represents impacts where such behavior is absent. A square  $(\blacksquare, \square)$  represents impacts where little rebound is present. Solid symbols (■) represent drops that do not break up, and symbols with a black outline  $(\Box)$  represent fragmented drops. We plot  $d_{h,s}$  versus  $\chi_s$  for hydrophobic fibers in Figure 4b and find that bouncing drops with zero final penetration cluster at around (0.85, 1.1), which indicates that they are nearly spherical,  $d_{\rm h.s} \lesssim 1 \lesssim \chi_{\rm s}$ , with a slight oblation under gravity. Further considerations of impact characteristics are given in the Supporting Information. The geometric measurements taken after impact show that impact classifications cluster in the post-impact parameter space but provide, at best, a convoluted prediction of the initial conditions of impact.

By considering an impact Weber number and modified aspect ratio  $AR^*$ , we find a superior predictor of impact behavior. We plot  $AR^*$  versus We for aligned fibers (A) in

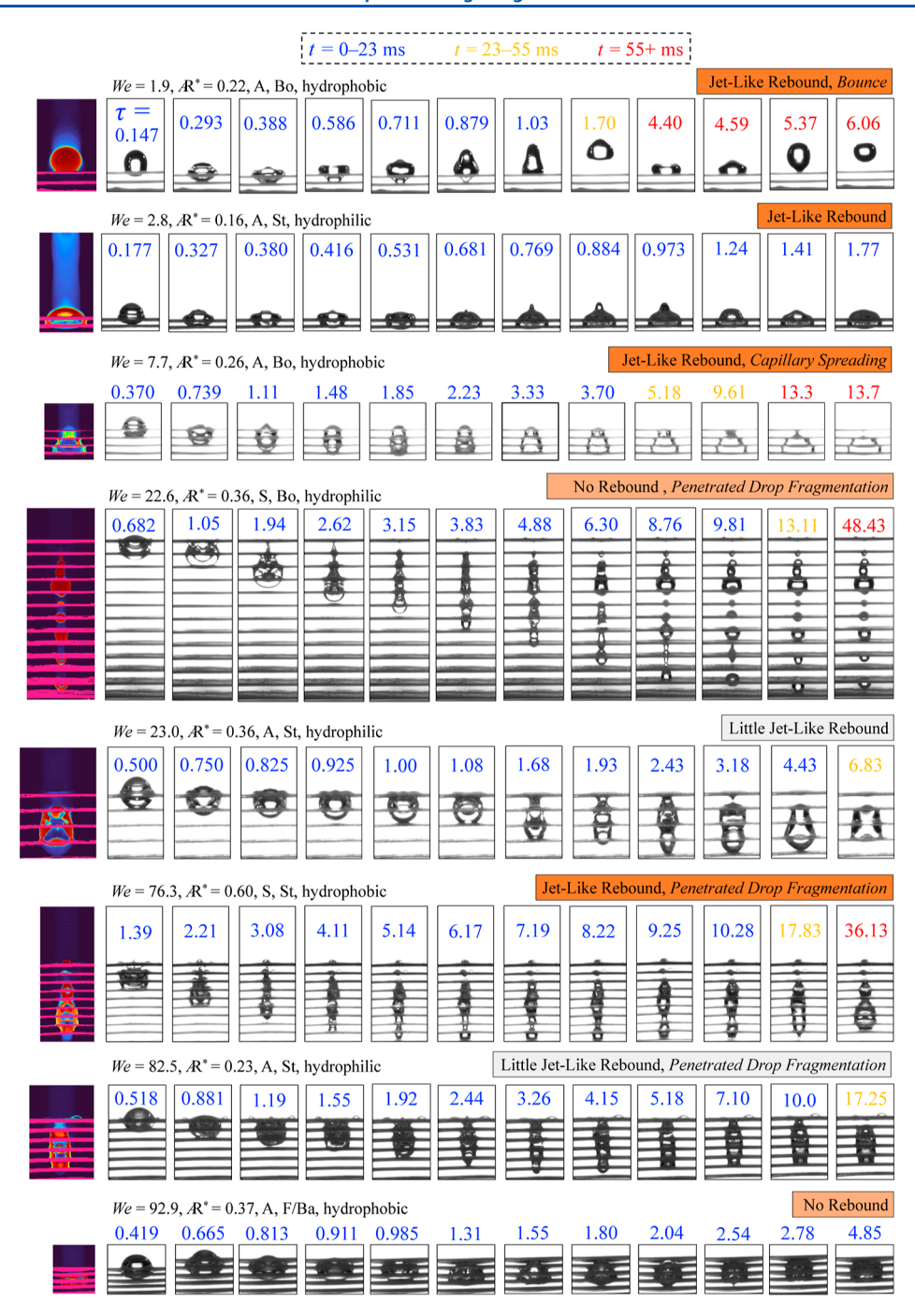


Figure 3. Image sequences of observed impact classifications, arranged in increasing We. The leftmost column shows normalized, temporal heat maps that quantify drop residence time and provide a characteristic image for each impact. Impact classification names are highlighted with a color based on rebound. Dimensionless time stamps in each frame ( $\tau$ ) are color-coded based on dimensional time. Refer to Table 2 for fiber configuration and orientation abbreviations.

Figure 5. Staggered fibers (S) exhibit very similar grouping in the  $AR^* - We$  space but are excluded in Figure 5 for the sake of clarity. Rebound is more likely to occur in lower  $AR^*$  and We values. Hydrophobicity induces drop bouncing at sufficiently low We, as shown in Figure 5b,d, but at higher We, fragmentation is promoted by hydrophobicity. Fibers with their wedge-like surface facing the drop, in bottom orientation (Bo, Figure 1c), likewise promote drop fragmentation. Fragmentation allows child droplets to penetrate further into the array than intact drops. We explore the relation between fragmentation and penetration in more detail in Hydro-

phobicity Promotes Penetration through Fragmentation. The penetration of fiber arrays by impacting drops and drop fragmentation is, unsurprisingly, greatest for the least dense arrays and fastest drops.

**Penetration.** Dense, Staggered Fibers Inhibit Penetration. By applying the conservation of energy on the drop before and after impact, a relationship between the maximum penetration depth  $d_{\rm p,m}$  and We may be attained. A pre- and post-impact energy balance takes the form

$$E_{\rm K} + E_{\rm S} + E_{\rm P} = E_{\rm S}' + E_{\rm D}' + E_{\rm P}'$$
 (4)

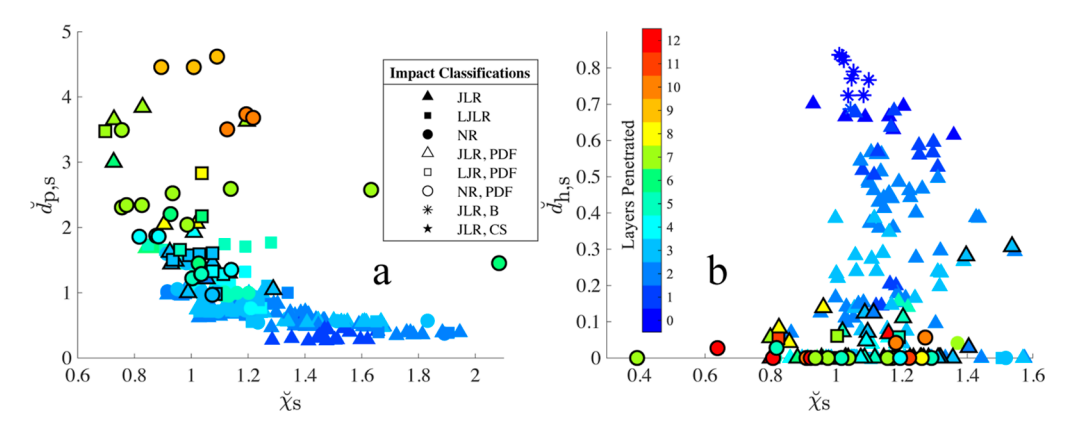


Figure 4. Geometric measurements of steady-state liquid mass after impact, normalized by drop diameter. (a) Normalized penetration depth  $d_{p,s}$  versus normalized lateral spread  $\check{\chi}_s$  for all trials onto hydrophilic fibers. (b) Normalized dome height  $\check{d}_{h,s}$  versus normalized lateral spread for all trials onto hydrophilic fibers. Refer to Table 2 for impact classification abbreviations. Solid symbols ( $\blacksquare$ ) represent drops that do not break up, and symbols with a black outline ( $\square$ ) represent fragmented drops.

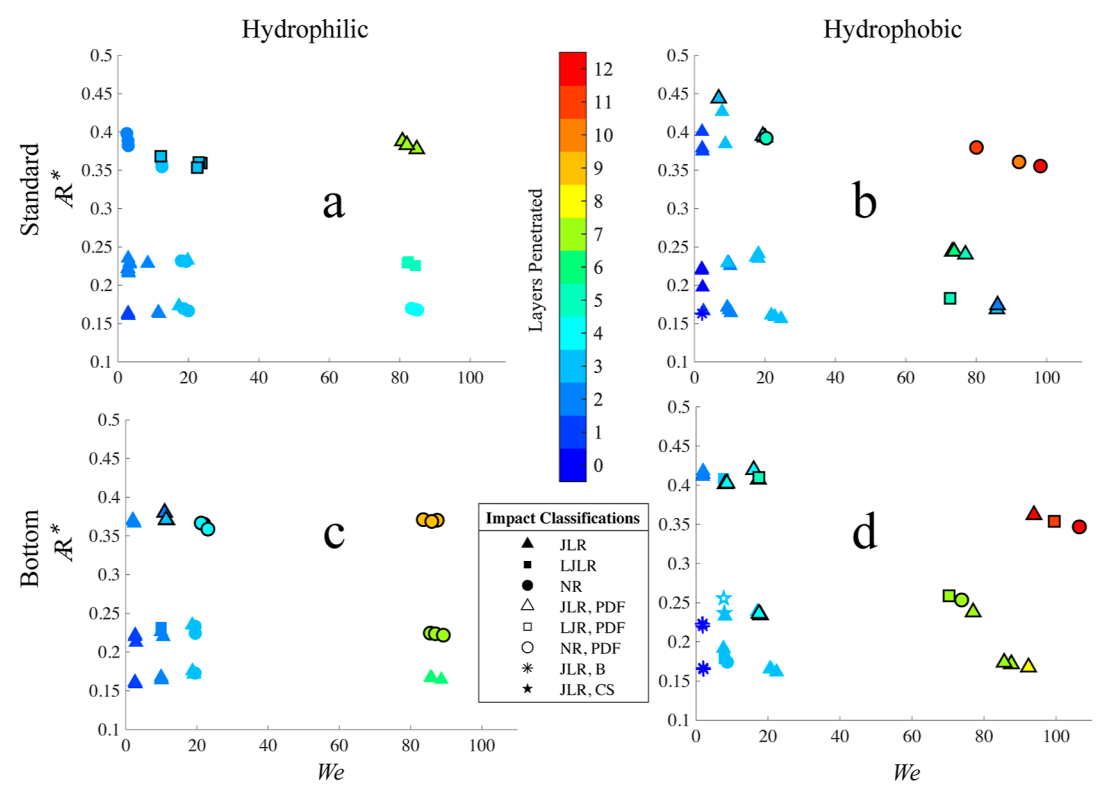


Figure 5. Modified fiber aspect ratio and Weber number drive impact classification. (a–d) Modified aspect ratio versus Weber number plot of aligned fiber arrays. All subplots in the higher row use fibers in standard orientation, whereas all in the lower row use fibers in bottom orientation. All subplots in the left column use hydrophilic fibers, whereas all in the right use hydrophobic fibers. Refer to Table 2 for classification abbreviations. The Supporting Information contains  $AR^*$  versus We plots for staggered fibers, Figure S1, and orientations are not shown here, Figure S2.

where  $E_{\rm K} = \pi \rho D_0^3 U^2/12$  is the kinetic energy at impact,  $E_{\rm S} = 4\pi D_0^2 \sigma$  is the surface energy of a spherical drop, and  $E_{\rm P}$  is the initial gravitational potential energy of the impacting drop, whereas  $E_{\rm S}'$  is the total final surface energy of the penetrated drop or fragments,  $E_{\rm D}'$  is the energy dissipated during impact, and  $E_{\rm P}'$  is the final gravitational potential energy of the penetrated drop or droplet fragments. One centimeter tall arrays ensure that  $E_{\rm P} \approx E_{\rm P}'$ .

Viscous dissipation during impact can be decomposed into two components, (1) shear forces on the vertically extruded liquid and (2) spreading of the drop bulk laterally on the topmost fiber row. On a no-slip surface, viscous dissipation occurs as the liquid undergoes shear within the boundary layer <sup>79</sup> with the time-scale of deformation  $\tau \approx D_0/U$  equal to our inertial time. <sup>80</sup> Using stagnation point flow, the boundary layer can be approximated to be of thickness <sup>58,80,81</sup>  $\delta = 2D_0/\sqrt{R}$ . The viscous dissipation per unit mass is  $\Phi = \mu(\partial v_i/\partial x_j + \partial v_j/\partial x_i)\partial v_i/\partial x_j \approx \mu U^2/\delta^2$ . The volume of the boundary layer is approximated by considering the deformation of a drop into n rectangular plates that vertically extrude between stacked fibers. We model this process as the flattening of a drop of diameter  $D_0$  to rectangular plates of width  $\chi_s$  and length  $d_{p,s}$ , as illustrated in Figure 6a, and thickness equivalent

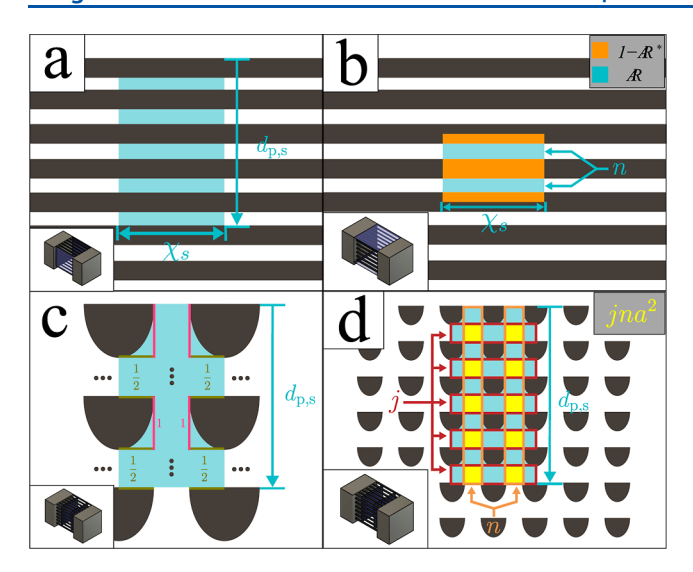


Figure 6. Graphical accompaniment to penetration depth model. Fibers are assumed square in our model. The view of fibers shown in each panel is indicated by the lightly colored planes in each inset. (a) Front and back view of the fiber array with the penetrated drop as seen by the camera. (b) Top and bottom view of the fiber array with the penetrated drop. AR is the fraction of drop projection that is in contact with air, whereas 1 - AR is the fraction that is occupied by fibers. (c) Cross-sectional view of the penetrated drop within the fiber array. The liquid body interacts with 4 sides of each fiber strand it encapsulates. Strands on the periphery are assumed to be wetted on 2 sides (1 complete side and 2 half-sides). (d) Cross-sectional view of the fiber array with the penetrated drop. The total intersection area of the horizontal plates and vertical plates, shown in yellow, is  $jna^2$ .

to the interfiber spacing a. Each liquid plate experiences shear on two sides from fiber contact according to the fraction 1-AR, as shown in Figure 6b. Thus, for each rectangular plate, the volume of fluid over which dissipation takes place can be approximated by  $\Omega \approx \chi_s d_{p,s}(2\delta)(1-AR)$ ; the boundary layer on each side of the liquid plate that is interacting with assumed square fibers is highlighted in pink in Figure 6c, and the area of each plate is illustrated in Figure 6a. The dissipation  $E_{D1}$  within the drop due to shear-induced by no-slip is

$$E'_{\rm D1} = n \int_0^{\tau} \int_{\Omega} \Phi \, d\Omega \, dt \approx n \Phi \Omega \tau \tag{5}$$

Substituting the  $\Phi,\,\Omega,$  and  $\tau$  and simplifying in terms of R

$$E'_{\rm D1} \approx n \chi_{\rm s} d_{\rm p,s} \mu U \sqrt{R} (1 - AR) \tag{6}$$

The remainder of the dissipation  $E'_{\rm D2}$  arises from vortical motions as the drop spreads laterally across the topmost fibers. On a solid surface,  $E'_{\rm D2}$  is equal to half of the initial kinetic energy. For a porous medium,  $E'_{\rm D2}$  only occurs on the areas occupied by solid fibers 1-AR, as illustrated in Figure 6b, and not on the empty spaces so that

$$E'_{\rm D2} \approx \frac{1}{2} (1 - AR) E_{\rm K}$$
 (7)

When  $AR \rightarrow 0$  in eq 7, formula for the case of solid surface is recovered. The total dissipation is

$$E'_{\rm D} = E'_{\rm D1} + E'_{\rm D2} \tag{8}$$

Using eqs 6 to 8, we find that  $E'_D$  is at least 1 order of magnitude lower than the total preimpact energy  $E_K + E_S$  so that  $E'_D$  can be neglected. On a solid surface, half of the kinetic

energy is dissipated mostly as the drop deforms and flattens; however, within a fiber array, there is reduced perpendicular redirection of drop motion such that a greater fraction of the initial kinetic and surface energy is converted into surface energy as the drops attach to greater total surface area within the fiber array. Thus, eq 4 can be simplified

$$E_{\rm K} + E_{\rm S} \approx E_{\rm S}^{\prime} \tag{9}$$

which is perhaps unsurprising in light of the magnitude of impact Re\*  $\approx 100-2000$ .

Nonbouncing, nonfragmented drops that fully penetrate have a total surface area that is proportional to the final penetration depth  $d_{p,s}$ , final spread width  $\chi_{s}$ , and the number of rectangular plates n. The surface energy due to the interaction of the liquid with the fiber surfaces within the array is approximately  $4n\chi_s d_{p,s}(1-AR)\sigma(1-\cos\theta)$ ; the factor 4 accounts for the 4 sides of every fiber strand, as shown in Figure 6c, and 1 - AR is the fraction of the fiber in the plate area  $\chi_s d_{p,s}$ . On the front and back sides (camera view) of the penetrated liquid illustrated in Figure 6a, the surface energy due to the interaction of the liquid with air is  $n\chi_s d_{p,s}AR\sigma$  on each side. On the top and bottom sides of the penetrated liquid illustrated in Figure 6b, the surface energy due to liquid-air interaction is  $na\gamma_s\sigma$  on each side. On the left and right sides (axial view) of the penetrated liquid illustrated in Figure 6d, the surface energy due to liquid-air interaction is  $[nad_{p,s} + jan(l+a) - jna^2]\sigma = nad_{p,s}(2 - AR)\sigma$  on each side, where  $j = d_{p,s}/(l + a)$  is the number of levels within the fiber array that is penetrated by the water drop. Thus, eq 9

$$\frac{\pi}{12}\rho D_0^3 U^2 + \pi D_0^2 \sigma$$

$$\approx 4n\chi_s d_{p,s} (1 - AR)\sigma (1 - \cos\theta) + 2n\chi_s d_{p,s} AR\sigma$$

$$+ 2na\chi_s \sigma + 2nad_{p,s} (2 - AR)\sigma \tag{10}$$

and is derived assuming square fibers. Rearranging eq 10

$$\frac{\pi}{12} \rho D_0^3 U^2 + \pi D_0^2 \sigma 
\approx 2\sigma n \{ [2(1 - \cos \theta) \chi_s d_{p,s} + a d_{p,s}] (1 - AR) 
+ \chi_s d_{p,s} AR + a (d_{p,s} + \chi_s) \}$$
(11)

which may be reasonably approximated by neglecting  $a(d_{\rm p,s}+\chi_{\rm s})$  and, since  $ad_{\rm p,s}\ll 2(1-\cos\theta)\chi_{\rm s}d_{\rm p,s}$ , can further be simplified to

$$\frac{\pi}{12} \rho D_0^3 U^2 + \pi D_0^2 \sigma$$

$$\approx 2\sigma \chi_{\rm s} d_{\rm p,s} [2n(1 - \cos \theta)(1 - AR) + AR] \tag{12}$$

and rewritten as

$$\frac{\pi}{12}\rho D_0^3 U^2 + \pi D_0^2 \sigma$$

$$\approx 4n\sigma \chi_s d_{p,s} (1 - \cos \theta) \left\{ 1 - \left[ 1 - \frac{1}{2n(1 - \cos \theta)} \right] AR \right\}$$
(13)

which is approximately

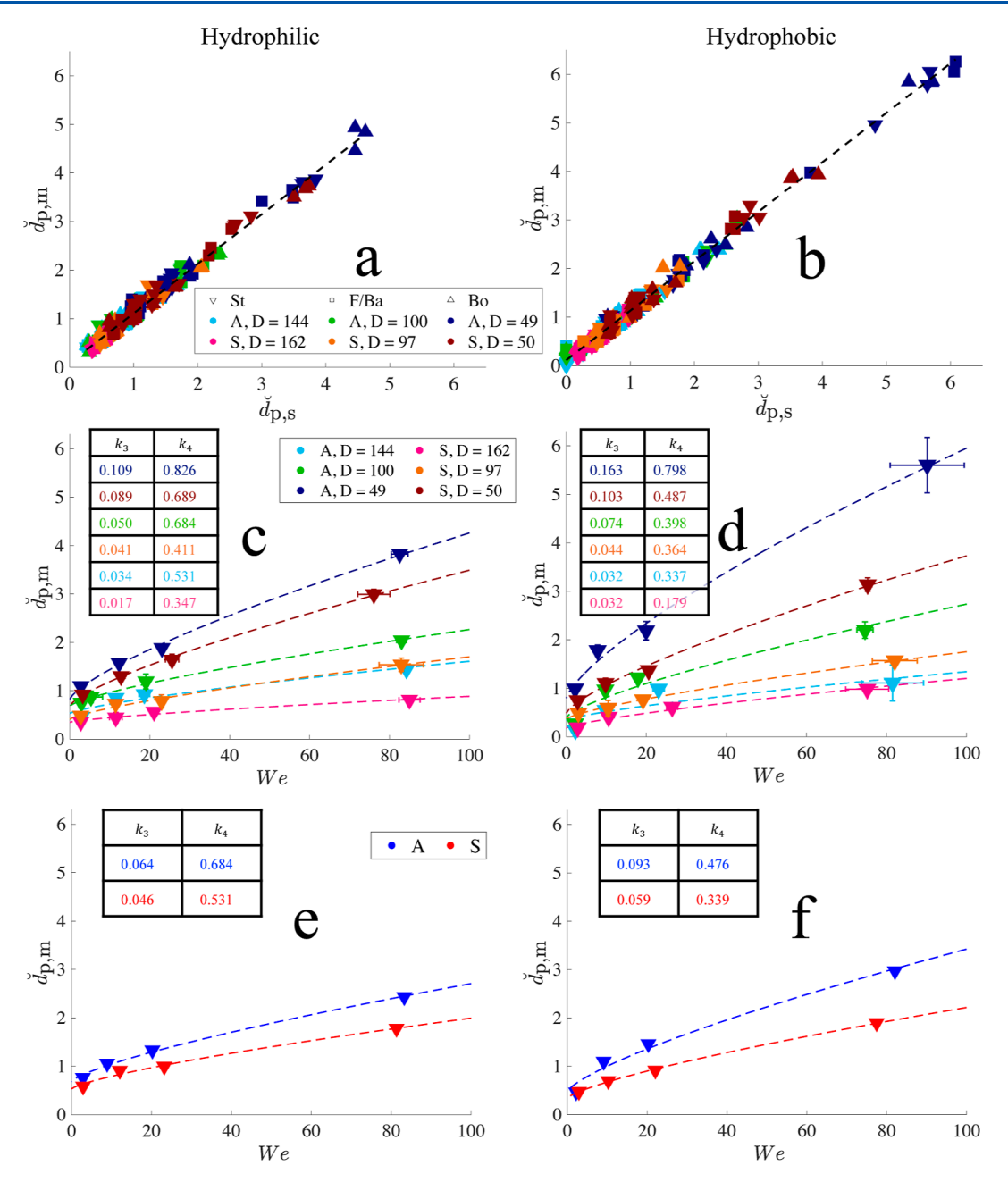


Figure 7. Normalized penetration depth. (a,b) Normalized maximum penetration depth versus normalized steady-state penetration depth. (c,d) Normalized maximum penetration depth versus Weber number in fibers in standard orientation. (e,f) Averaged curves for aligned and staggered fibers in e and f. Dashed lines represent power law curve fits generated using eq 24. Fiber density (D) numbers in strands/cm<sup>2</sup>; St = standard, F/Ba = front/back, Bo = bottom; A = aligned, S = staggered; refer to Table 2. All subplots in the left column use hydrophilic fibers, whereas all in the right use hydrophobic fibers.

$$\frac{\pi}{12} \rho D_0^{\ 3} U^2 + \pi D_0^2 \sigma \approx 4n\sigma \chi_s d_{p,s} (1 - \cos \theta) (1 - AR)$$
(14)

It has been shown that the spreading of a drop impacting single fibers  $^{29}$  and solid surfaces  $^{82}$  obeys

$$\chi_{\rm s} = c_1 W e^{1/4} + D_0 \tag{15}$$

where  $c_1$  is a positive constant. Moreover, from geometry

$$n \propto D_0/(l+a) \tag{16}$$

Combining eqs 14 to 16

$$\frac{\pi}{12}\rho D_0^3 U^2 + \pi D_0^2 \sigma$$

$$\propto 4 \frac{D_0}{l+a} \sigma (c_1 W e^{1/4} + D_0) d_{p,s} (1 - \cos \theta) (1 - AR)$$
(17)

Using our definition of We and rearranging eq 17

$$\frac{\pi D_0}{48(1 - \cos\theta)(1 - AR)c_1} \frac{We}{We^{1/4} + \frac{D_0}{c_1}} + \frac{\pi D_0}{4(1 - \cos\theta)(1 - AR)c_1 \left(We^{1/4} + \frac{D_0}{c_1}\right)} \propto \frac{d_{p,s}}{l + a} \tag{18}$$

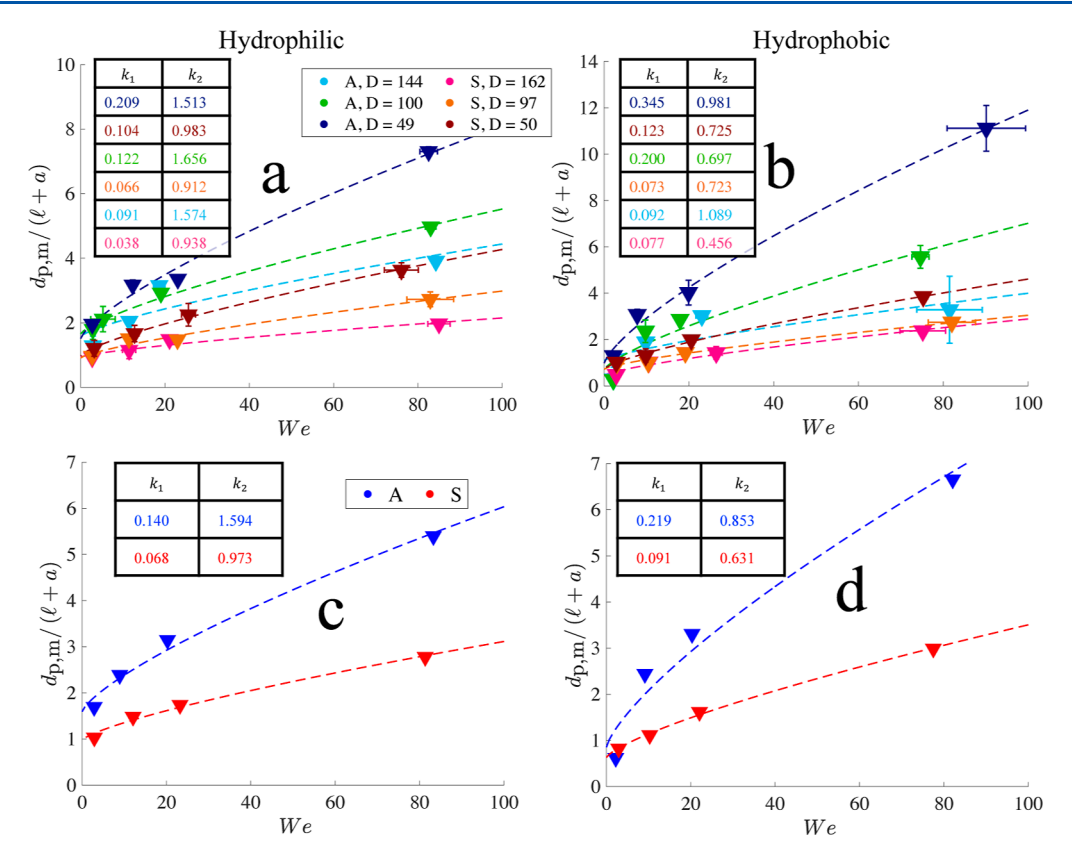


**Figure 8.** Characteristic penetration depth. (a,b) Characteristic maximum penetration depth versus Weber number in fibers in standard orientation. (c,d) Averaged curves for aligned and staggered fibers in e and f. Dashed lines represent power law curve fits generated using eq 24. Fiber density (D) numbers in strands/cm<sup>2</sup>; St = standard, F/Ba = front/back, Bo = bottom; A = aligned, S = staggered; refer to Table 2. All subplots in the left column use hydrophilic fibers, whereas all in the right use hydrophobic fibers.

ı

For dynamic drop impacts at high We values when  $We^{1/4} \gg D_0/c_1$ , the leftmost term in eq 18 is dominant, and eq 18 is approximately equivalent to

$$\frac{\pi D_0}{48(1 - \cos\theta)(1 - AR)c_1} We^{3/4} \sim \frac{d_{p,s}}{l + a}$$
for  $We \gg 53$  (19)

An estimate of  $D_0/c_1=2.7$  for nonwedged fibers with  $I/D_0=0.4$  can be found on a previous drop impact onto pine needle fibers. Such an estimate can be used as a preliminary basis, but further experiments should be conducted to obtain a better estimate for  $D_0/c_1$  for lower  $I/D_0$  values. Using such an estimate, the previously mentioned condition for eq 19 is thus satisfied when  $We^{1/4}\gg 2.7$ , or equivalently, when  $We\gg 53$ . Otherwise, for static drops at low We values when  $We^{1/4}\ll D_0/c_1$ , the rightmost term in eq 18 is dominant and eq 18 is approximately equivalent to

$$\frac{\pi}{4(1-\cos\theta)(1-AR)} \sim \frac{d_{\rm p,s}}{l+a} \qquad \text{for } We \ll 7.3$$
(20)

a validity condition that appears by comparing the magnitudes of the dynamic (eq 19) and static (eq 20) components of penetration. Therefore, the retention of both static and dynamic components is appropriate for  $7.3 \lesssim We \lesssim 53$ .

We now introduce a "characteristic penetration depth" that is relative to the fiber size and spacing

$$\frac{d_{\mathbf{p}}}{l+a} = \breve{d}_{\mathbf{p}} \frac{D_0}{l+a} \tag{21}$$

Combining eqs 19 and 20, we may write

$$\frac{d_{p,s}}{l+a} = k_1 W e^{3/4} + k_2 (22)$$

where the two non-negative coefficients are  $k_1 \sim (\pi D_0)/[48(1-\cos\theta)(1-AR)c_1]$  and  $k_2 \sim \pi/[4(1-\cos\theta)(1-AR)]$ . The coefficient  $k_1$  represents the strength of kinetic energy, and the static coefficient  $k_2$  represents the initial surface energy together with auxiliary effects such as capillary-driven penetration and the penetration of fragments through the fiber interstices. Similarly, from eq 21

$$d_{p,s} = k_3 W e^{3/4} + k_4$$
(23)

with non-negative coefficients  $k_3 = k_1(l+a)/D_0 \sim \pi(l+a)/[48(1-\cos\theta)(1-AR)c_1]$  and  $k_4 = k_2(l+a)/D_0 \sim \pi(l+a)/[4(1-\cos\theta)(1-AR)D_0]$ . The negative correlation between AR and the penetration depth coefficients  $k_1$  and  $k_2$  imply that denser fibers inhibit penetration. As  $AR \rightarrow 0$ , fiber density increases: the interstitial spaces within the array shrink so that the array becomes more solid, and the penetration depth coefficients approach a minimum value. Conversely, as  $AR \rightarrow 1$  fiber density decreases, the array behaves as single fiber, and the penetration depth coefficients approach infinity. At low velocity, we expect  $k_2 > k_1We^{3/4}$  for hydrophilic fibers where capillarity is significant. In static drops, We = 0 but penetration can still occur due to capillary action  $(k_2 \ge 0)$ .

To this point, we have considered penetration depth as the maximum achieved by impacting drop. However, drops often retract such that their final resting depth  $\check{d}_{p,s} < \check{d}_{p,m}$ . For hydrophilic fibers,  $\check{d}_{p,s}/\check{d}_{p,m}=0.90$ , whereas  $\check{d}_{p,s}/d_{p,m}=0.84$  for hydrophobic fibers, as shown in Figure 7a,b. The lower  $\check{d}_{p,s}/\check{d}_{p,m}$  ratio in hydrophobic fibers is a result of more prominent vertical drop retraction at low We, often resulting in the drop bouncing and subsequently a zero final resting depth. Nevertheless, the linear functions fit to the data in Figure 7 have very similar slopes for hydrophilic (1.020) and hydrophobic fibers (1.018). Therefore, the use of  $\check{d}_{p,m}$  or  $\check{d}_{p,s}$  as well as of  $d_{p,m}/(l+a)$  or  $d_{p,s}/(l+a)$  is nearly equivalent. Thus

$$\begin{split} \frac{d_{\rm p,m}}{l+a} &\approx \frac{d_{\rm p,s}}{l+a} = k_1 W e^{3/4} + k_2 \quad \text{and} \\ \check{d}_{\rm p,m} &\approx \check{d}_{\rm p,s} = k_3 W e^{3/4} + k_4 \end{split} \tag{24}$$

We plot the normalized maximum penetration depth  $d_{p,m}$  versus We for all fiber densities and alignments in Figure 7c,d, whereas the characteristic maximum penetration depth  $d_{p,m}/(l+a)$  is plotted versus We in Figure 8a,b. Symbols with blue spectrum colors represent impacts with aligned fibers, whereas staggered fiber impacts are of the red spectrum. Orientation is differentiated by symbol shape: standard (St) orientation by  $\nabla$ , front/back (F/Ba) orientation by  $\square$ , and bottom (Bo) orientation by  $\triangle$ , refer to Table 2. When using

Table 2. Legend Labels

abbreviation	definition
D	fiber density in strands/cm <sup>2</sup>
A	aligned fiber configuration, refer to Figure 1
S	staggered fiber configuration, refer to Figure 1
St	"standard" fiber orientation, refer to Figure 1
F/Ba	"front/back" fiber orientation, refer to Figure 1
Во	"bottom" fiber orientation, refer to Figure 1
JLR	jet-like rebound, refer to Figure 3
LJLR	little jet-like rebound, refer to Figure 3
NR	no rebound, refer to Figure 3
JLR, CS	jet-like rebound, capillary spreading, refer to Figure 3
JLR, B	jet-like rebound, bounce, refer to Figure 3
PDF	penetrated drop fragmentation, refer to Figure 3

the characteristic penetration depth, as shown in Figure 8, the effect of the staggered configuration in lowering the value of  $d_{\rm p,m}/(l+a)$  is emphasized so that the normalized penetration depth  $\check{d}_{\rm p,m}$  is the appropriate variable to use when comparing penetration depth across different fiber types. As expected, denser fibers have lower penetration depth coefficients  $k_1, k_2$  or  $k_3, k_4$ , as shown in Figures 8a,b and 7c,d. Considering that the fiber density used in this work is 2 to 4 orders of magnitude lower than typical animal furs, <sup>13</sup> we posit that as fur density grows past what we can manufacture, toward the density of typical animal furs, the penetration depth of falling drops into fibrous arrays will approach a functionally zero penetration depth. Thus, we expect the skin of many mammals to remain dry in the most violent rainfall.

To isolate the influence of configuration on penetration depth, we average the  $d_{\rm p,m}/(l+a)$  and  $\check{d}_{\rm p,m}$  for each Weber number in Figures 8a,b and 7c,d and plot the result in Figures 8c,d and 7e,f. For both wetting conditions, penetration is inhibited by the staggered fiber configuration, as expected.

Such greater resistance to penetration of staggered fibers is reflected by a lower  $k_3$  and  $k_4$  in Figure 7. On average, at  $We \approx 80$ , staggered fibers reduce penetration by 24% in hydrophilic fibers and 34% in hydrophobic fibers, and the penetration reduction percentage is expected to increase with increasing We, as evidenced by Figure 7e,f. Mammals benefit from such wetting-resistant properties of staggered fibers. Hair follicles of mammalian furs classified as having single follicles versus compound follicles are typically arranged in staggered rows.  $^{83-85}$  In mammals where a primary single follicle coexists with several secondary compound follicles, the primary and secondary follicles are arranged in staggered rows as in rats and mice.  $^{83,84}$  The primary follicle may instead be randomly distributed within the finer secondary follicles.  $^{83,86,87}$ 

Hydrophobicity Promotes Penetration through Fragmentation. With an average dynamic coefficient ( $k_3 = 0.0746$ ) that is 32% higher than their hydrophilic counterpart ( $k_3 = 0.0565$ ), hydrophobic fibers experience greater penetration depths at higher drop velocities than hydrophilic fibers, as shown in Figure 7c,d. In contrast, hydrophilic fibers experience greater penetration depths at lower drop velocities with an average static coefficient ( $k_4 = 0.581$ ) that is 36% higher than their hydrophobic counterpart ( $k_4 = 0.427$ ). At low We, the reduced capillarity in hydrophobic fibers prevents low-speed wicking. However, at higher We, capillarity in hydrophilic fibers encourages the drop to spread laterally, thereby inhibiting penetration. Aligned fibers of density 49 strands/cm<sup>2</sup> have higher  $k_4$  in hydrophobic fibers than their hydrophilic counterpart due to early fragmentation starting at low We values, as can be verified in Figure 5a,b. Fragmentation is enhanced by a combination of fiber hydrophobicity and low fiber density and is captured in  $k_4$ . We therefore posit that hydrophobic fur will resist water penetration more effectively when brushing by a wet plant, whereas hydrophilic fur performs better when drops are inertial. The lower  $k_4$  of hydrophobic fibers allows for a functionally zero final penetration depth if the We is sufficiently low, in which cases drops bounce (Figure 3). A critical Weber number We<sub>c</sub> at which the penetration depth of hydrophobic fibers exceeds that of their hydrophilic counterparts is printed on the plots of Figure 9, a critical value that is dependent on array properties. We aggregate  $We_c$  and plot versus array density D in Figure 10. Staggered fibers have higher Wec than their aligned counterparts, and the disparity in Wec is reduced by wedgeness as the orientation changes from standard to front/back and bottom. Such disparity tends to decrease with increasing density in the standard and bottom orientations, where symmetry exists in the sagittal plane of the fiber strand cross-section (Figure 1). In contrast, where such sagittal symmetry does not exist such as in the front/back orientation, the disparity grows with increasing density. Interestingly, We<sub>c</sub> is independent of fiber orientation and is not correlated with density.

Drop fragmentation increases the penetration depth of water on fiber arrays, as shown in Figure 5a. Thus, understanding the basis of drop fragmentation will provide insights into the factors that aid and inhibit penetration. Higher We and  $AR^*$  enhance drop penetration and fragmentation, as mentioned in Impact Classifications and as shown in Figure 5c,d, so that an increase in We may be compensated by a decrease in  $AR^*$  and vice versa. The product of We and  $AR^*$  is thus a useful indicator of drop impact behavior. A similar approach has been used in previous works. <sup>74,75</sup> In textile fibers, for example, it was found that the critical mesh size to prevent penetration is

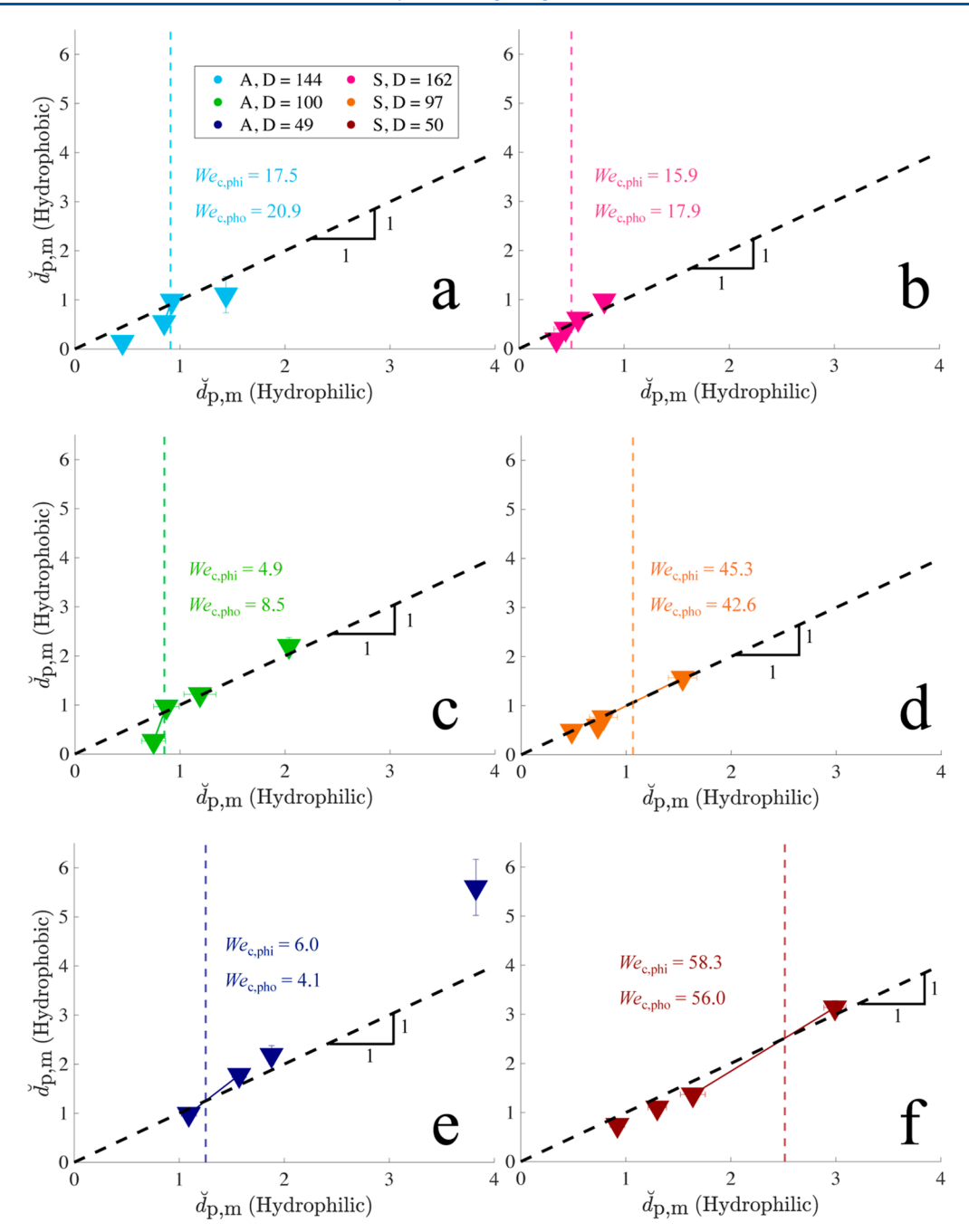
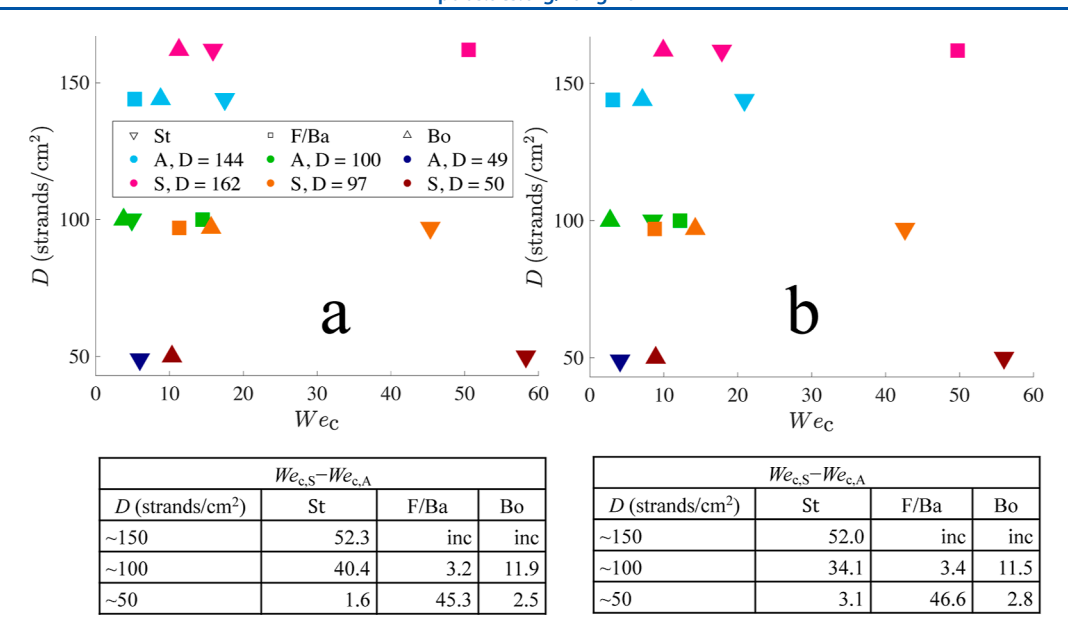


Figure 9. (a–f) Normalized maximum penetration depth in hydrophobic fibers versus the same quantity in hydrophilic fibers. Vertical lines indicate the critical We where the penetration depth in hydrophobic fibers starts exceeding the corresponding value in hydrophilic fibers. We interpolated from experimental data points of hydrophilic ( $We_{c,phi}$ ) and hydrophobic ( $We_{c,pho}$ ) fibers. Fiber density (D) numbers in strands/cm<sup>2</sup>; A = aligned, S = staggered; refer to Table 2.

inversely proportional<sup>74</sup> to the We, textile mesh size is analogous to  $AR^*$  in this work. Hydrophobic textiles are known to break water drops into secondary droplets.<sup>57</sup>

In our work, it can be seen that hydrophobicity enhances fragmentation at higher drop velocities when fibers are aligned as evidenced in Figure 5, allowing hydrophobic fibers to experience greater penetration depth by impacting drops, as shown in Figure 9. Fragmentation becomes more likely as We  $AR^*$  increases, as illustrated in Figure 11. Solid symbols ( $\blacksquare$ ) in Figure 11 represent drops that do not break up, and symbols with a black outline ( $\square$ ) represent fragmented drops. Moreover, the critical We  $AR^*$  value beyond which

fragmentation begins to occur increases from around 3 to 5 as the configuration changes from aligned to staggered, as shown in Figure 11a—d, demonstrating how the staggered configuration helps prevent drop fragmentation and reduce penetration. The wedge-like shape in the bottom orientation also promotes drop fragmentation when fibers are aligned regardless of fiber hydrophilicity, as shown by comparing Figure 5a,b with Figure 5c,d, and generally in hydrophilic fibers regardless of fiber alignment, as shown by comparing Figure 11e with Figure 11i, an observation consistent with impacts onto single, wedged fibers.<sup>29</sup> However, a wedge-like shape also promotes capillary spreading, which, as discussed in Hydro-



**Figure 10.** Array density D versus critical Weber number  $We_c$  of (a) hydrophilic and (b) hydrophobic fibers. Corresponding tables show differences in  $We_c$  values between staggered ( $We_{c,S}$ ) and aligned fibers ( $We_{c,A}$ ); in cases where a crossing event for  $We_c$  is inconclusive in the hydrophilic or hydrophobic counterpart, "inc" is written. St = standard, F/Ba = front/back, Bo = bottom; A = aligned, S = staggered; refer to Table 2.

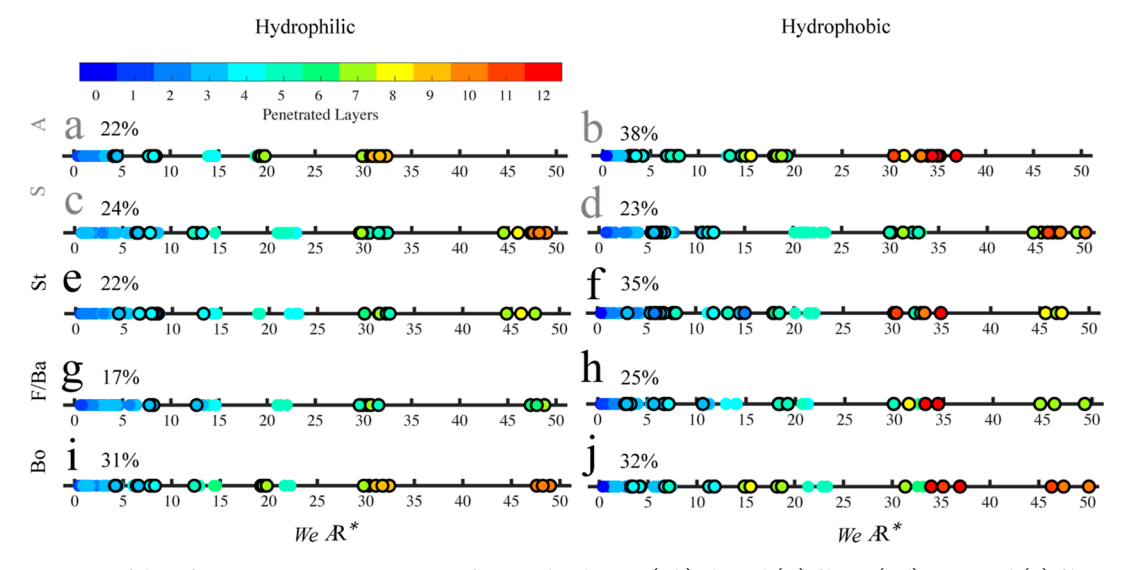


Figure 11. Occurrence of drop fragmentation across a range of  $We\ AR^*$  values in (a,b) aligned (A) fibers, (c,d) staggered (S) fibers, (e,f) fibers in standard (St) orientation, (g,h) fibers in front/back (F/Ba) orientation, and (i,j) fibers in bottom (Bo) orientation; refer to Table 2. Solid symbols ( $\blacksquare$ ) in figure represent drops that do not fragment, and symbols with a black outline ( $\square$ ) represent fragmented drops. Plots a—d include data from all orientations. Plots e—j include data from all fiber configurations. All subplots in the left column use hydrophilic fibers, whereas all in the right use hydrophobic fibers. The percentage of drop fragmentation is shown beside the letter for each subplot.

phobicity Promotes Penetration through Fragmentation, inhibits penetration. Thus, the influence of the cross-sectional shape of an array on the penetration depth is complex and an area for future work.

Implications for Mammals and Applications. We posit that hydrophilic fibers resist raindrop infiltration more effectively than hydrophobic fibers based on our laboratory observation that hydrophobic fibers encourage fragmentation and inhibit spreading, thereby increasing the penetration depth of impacting drops. To this point in the study, we have considered drop velocities ranging from ~0.25 to ~1.5 m/s. However, raindrops can fall as fast as 9 m/s. While we are unable to generate 9 m/s drops in the lab, we film drops at >5 m/s to explore drop behaviors when drops impact with

sufficient energy to shatter. Image sequences of such high-speed impacts onto arrays of each wetting condition are shown in Figure 12a,b and correspond to Movie S5. Hydrophilic fibers arrest the drop, thereby inhibiting full penetration of the array. Hydrophobic fibers allow the drop to break into secondary droplets and penetrate to the floor of the array.

Our results suggest that guard hair in animal fur should be hydrophilic to be most effective at resisting infiltration by impacting drops, but data on fur wettability remains scarce. Sheep wool, which is known to be hydrophobic due to the lanolin secreted by the sebaceous glands of wool-bearing animals, <sup>89</sup> may stand as a clear exception due to the unique arrangement of curly wool fibers. Wool strands are intricately interlocked, thereby leaving no continuous path for liquid

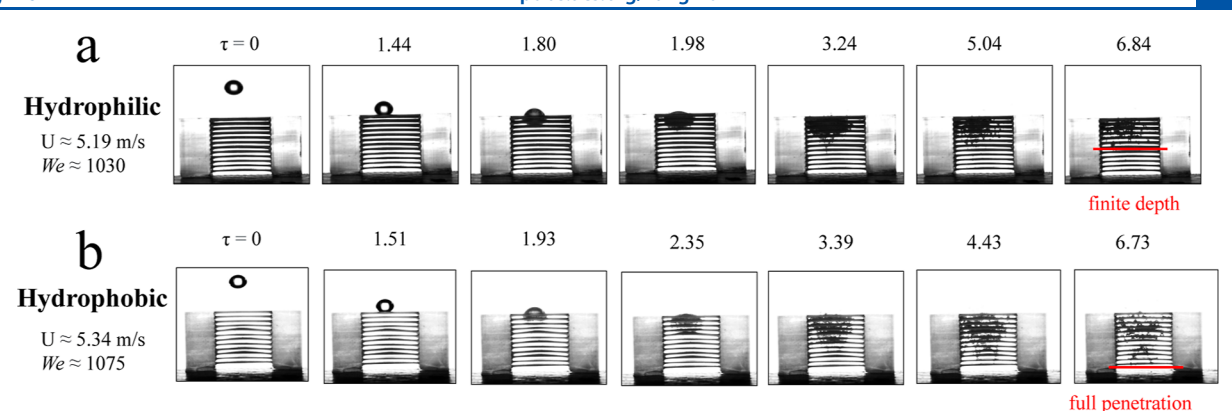


Figure 12. High-speed impact image sequences. Drop impacting (a) hydrophilic and (b) hydrophobic fibers at >5 m/s.

travel—hydrophobicity aids wools in resisting both static and dynamic water drop penetration. Moreover, we posit that animals that possess underfur, which is typically denser and shorter than guard hair, benefit from hydrophobic underfur to resist wicking to the skin. In nature, animal underfur strands are an order of magnitude thinner<sup>90</sup> and orders of magnitude denser<sup>91</sup> than guard hair strands. A hybrid composition—a hydrophilic outer layer and hydrophobic inner layer—may perhaps be optimal for resisting water infiltration and is an area for future work.

Our results may prove useful for applications in moisture and rainwater capture, 92 filtration of liquid sprays, 93 spray cooling, 94,95 and engineering surfaces that are resistant to water penetration but allow for gas exchange. The measurement of penetration depth into arrays similar to ours may be used to define distributions of drop size and velocity in rainfall and other types of sprays.

Future researchers may choose to improve our experimental system to more realistically mimic natural fur. Enhancement may include cantilevered fibers and the incorporation of an impact angle to investigate how the direction of the array governs penetration and spreading dynamics. Improvements in additive manufacturing will enable future arrays to approach the density of animal furs and incorporate the natural elliptical profiles they exhibit. 10 The number of drops in sequence at a single location is yet another variable that may be explored. We hypothesize that increasing the number of drops impacting a single location nonlinearly increases mass infiltration to a steady depth by saturating the outer layers of the array. The final step in complexity is the incorporation of locomotion dynamics on penetration and shedding of drops. Drop impacts on moving surfaces can be very different from impacts on static surfaces, as the degree of drop deformation and splashing is enhanced by surface tangential velocity. 47,58,63 Finally, we recommend improving the range of Ohnesorge numbers by adding glycerin, alcohol, and other inertial fluids to the water drops.

# CONCLUSIONS

In this paper, we establish that horizontally oriented hydrophilic fiber arrays provide greater resistance to dynamic penetration by falling drops than hydrophobic fibers, at the array densities tested, by promoting lateral drop spreading and inhibiting drop fragmentation. Hydrophobic fibers are superior in preventing static and low-speed infiltration. Using conservation of energy, we obtain a linear relationship between the normalized penetration depth of impacting drops and their

Weber number. A dynamic penetration coefficient  $k_1$  captures the influence of kinetic energy, and a static coefficient  $k_2$  captures auxiliary effects such as wicking. The  $k_1$  of hydrophobic fibers is higher than their hydrophilic counterparts, whereas the  $k_2$  of hydrophobic fibers is relatively lower. At impact velocities approaching those of raindrops, drops impacting hydrophobic arrays shatter into many small droplets that deeply penetrate the array. The difference in drop behaviors between our two wetting conditions will change with array density beyond that which we tested here. Denser hydrophobic arrays, for example, are more likely to induce complete rebound. Drops that do shatter will do so radially rather than into the array.

As expected, fiber density and staggering increase array resistance to penetration. Denser and staggered fibers have lower penetration depths  $d_p$  compared with sparser and aligned fiber counterparts. Restriction in vertical drop motion prevents variations in  $d_p$  so that steady-state and maximum penetration depths are nearly equivalent. Lateral spreading  $\check{\chi}$  restricts  $\check{d}_p$  in hydrophilic fibers.

#### ASSOCIATED CONTENT

#### Supporting Information

The Supporting Information is available free of charge at https://pubs.acs.org/doi/10.1021/acs.langmuir.4c00371.

Impact classifications and their associated temporal heat maps (MP4)

Drops impact aligned samples of density 144 strands/  $cm^2$  at a velocity  $\approx 0.5 m/s$  (MP4)

Drops impact aligned sample of density 144 strands/cm<sup>2</sup> at a velocity  $\approx 0.3 \text{m/s}$  (MP4)

Drops impact aligned samples of density 144 strands/ $cm^2$  at a velocity  $\approx 0.5 m/s$  with time annotations (MP4)

Drops at  $\sim$ 5 m/s impact hydrophilic and hydrophobic fibers (MP4)

Figures showing the rest of the modified aspect ratio versus Weber number plots that are not shown in Figure 5, and an additional section discussing auxiliary drop impact characteristics (PDF)

#### AUTHOR INFORMATION

# **Corresponding Author**

Andrew K. Dickerson – Department of Mechanical, Aerospace, and Biomedical Engineering, University of Tennessee, Knoxville, Tennessee 37996, United States; orcid.org/0000-0003-1220-1048; Email: dickerson@utk.edu

#### **Authors**

Gene Patrick S. Rible – Department of Mechanical, Aerospace, and Biomedical Engineering, University of Tennessee, Knoxville, Tennessee 37996, United States

Michael A. Spinazzola, III – Department of Mechanical, Aerospace, and Biomedical Engineering, University of Tennessee, Knoxville, Tennessee 37996, United States

Robert E. Jones, III – Department of Mechanical, Aerospace, and Biomedical Engineering, University of Tennessee, Knoxville, Tennessee 37996, United States

Rachel U. Constantin – Department of Mechanical, Aerospace, and Biomedical Engineering, University of Tennessee, Knoxville, Tennessee 37996, United States

Wei Wang — Department of Mechanical, Aerospace, and Biomedical Engineering, University of Tennessee, Knoxville, Tennessee 37996, United States; orcid.org/0000-0002-1260-2098

Complete contact information is available at: https://pubs.acs.org/10.1021/acs.langmuir.4c00371

#### Notes

The authors declare no competing financial interest.

# ACKNOWLEDGMENTS

This research was partially funded by the National Science Foundation (CMMI 1825801 and CBET 2153740). We thank undergraduate research assistants at the Fluids and Structures Laboratory, Visalsaya Chakpuang, David Job Dooley, and Agustin Soto for bespoke code contributions, Rachel Robinette for video analysis, and Syed Jaffar Raza for editing the supplementary videos. We also give special thanks to Mohammad Alipanahrostami for coating our hydrophobic fibers.

# REFERENCES

- (1) Madkour, F. A.; Abdelsabour-Khalaf, M. Performance scanning electron microscopic investigations and elemental analysis of hair of the different animal species for forensic identification. *Microsc. Res. Tech.* **2022**, 85 (6), 2152–2161.
- (2) Malhotra, M.; Nanhe, B. Sem studies on some animal hairs with reference to scale pattern and scale count. *J. Emerg. Technol. Innov. Res.* **2019**, *6*, 783–787.
- (3) Amador, G. J.; Hu, D. L. Cleanliness is next to godliness: mechanisms for staying clean. *J. Exp. Biol.* **2015**, 218 (20), 3164–3174.
- (4) Mota-Rojas, D.; Titto, C. G.; de Mira Geraldo, A.; Martínez-Burnes, J.; Gómez, J.; Hernández-Avalos, I.; Casas, A.; Domínguez, A.; José, N.; Bertoni, A.; et al. Efficacy and function of feathers, hair, and glabrous skin in the thermoregulation strategies of domestic animals. *Animals* **2021**, *11* (12), 3472.
- (5) Minakami, K.; Obara, T.; Yamauchi, C. The effects of fur on the thermal regulation of mice (mus musculus). *Exp. Anim.* **1986**, 35 (1), 101–105.
- (6) Murphrey, M. B.; Agarwal, S.; Zito, P. M. Anatomy, Hair; StatPearls, 2023.
- (7) Welle, M. M.; Wiener, D. J. The hair follicle: a comparative review of canine hair follicle anatomy and physiology. *Toxicol. Pathol.* **2016**, *44* (4), 564–574.
- (8) Dawson, T. J.; Webster, K. N.; Maloney, S. K. The fur of mammals in exposed environments; do crypsis and thermal needs necessarily conflict? The polar bear and marsupial koala compared. *J. Comp. Physiol. B* **2014**, *184*, 273–284.

- (9) Krsmanovic, M.; Biswas, D.; Ali, H.; Kumar, A.; Ghosh, R.; Dickerson, A. K. Hydrodynamics and surface properties influence biofilm proliferation. *Adv. Colloid Interface Sci.* **2021**, 288, 102336.
- (10) Krsmanovic, M.; Ali, H.; Biswas, D.; Ghosh, R.; Dickerson, A. K. Fouling of mammalian hair fibres exposed to a titanium dioxide colloidal suspension. *J. R. Soc. Interface* **2022**, *19* (189), 20210904.
- (11) Bakken, G. S. A heat transfer analysis of animals: unifying concepts and the application of metabolism chamber data to field ecology. *J. Theor. Biol.* **1976**, *60* (2), 337–384.
- (12) Boks, N. P.; Busscher, H. J.; van der Mei, H. C.; Norde, W. Bond-strengthening in staphylococcal adhesion to hydrophilic and hydrophobic surfaces using atomic force microscopy. *Langmuir* **2008**, 24 (22), 12990–12994.
- (13) Dickerson, A. K.; Mills, Z. G.; Hu, D. L. Wet mammals shake at tuned frequencies to dry. J. R. Soc. Interface 2012, 9 (77), 3208–3218.
- (14) Morano, C.; Dei Cas, M.; Bergamaschi, R. F.; Palmisano, E.; Pallavicini, M.; Bolchi, C.; Roda, G.; Casati, S. Fractioning and compared 1h nmr and gc-ms analyses of lanolin acid components. *Molecules* **2023**, 28 (4), 1635.
- (15) Weisel, J. W.; Nagaswami, C.; Peterson, R. O. River otter hair structure facilitates interlocking to impede penetration of water and allow trapping of air. *Can. J. Zool.* **2005**, 83 (5), 649–655.
- (16) Mason, W. K. Investigating epizoochorous adaptations to mammalian furs. Ph.D. Thesis, Department of Biology; University of Winnipeg, 2004.
- (17) Zhu, P.; Wang, W.; Chen, X.; Lin, F.; Wei, X.; Ji, C.; Zou, J. Experimental study of drop impact on a thin fiber. *Phys. Fluids* **2019**, 31 (10), 107102.
- (18) Zhang, H.; Yi, X.; Du, Y.; Zhang, R.; Zhang, X.; He, F.; Niu, F.; Hao, P. Dynamic behavior of water drops impacting on cylindrical superhydrophobic surfaces. *Phys. Fluids* **2019**, *31* (3), 032104.
- (19) Tang, Y.-Y.; Su, M.-J.; Chu, G.-W.; Luo, Y.; Wang, Y.-Y.; Zhang, L.-L.; Chen, J.-F. Impact phenomena of liquid droplet passing through stainless steel wire mesh units. *Chem. Eng. Sci.* **2019**, *198*, 144–154.
- (20) Aziz, H.; Farhan, N. M.; Tafreshi, H. V. Effects of fiber wettability and size on droplet detachment residue. *Exp. Fluid* **2018**, 59, 122.
- (21) Safavi, M.; Nourazar, S. S. Experimental, analytical, and numerical study of droplet impact on a horizontal fiber. *Int. J. Multiphase Flow* **2019**, *113*, 316–324.
- (22) Kim, S.-G.; Kim, W. Drop impact on a fiber. *Phys. Fluids* **2016**, 28 (4), 042001.
- (23) Wang, Y. Numerical study of a droplet impact on cylindrical objects: towards the anti-icing property of power transmission lines. *Appl. Surf. Sci.* **2020**, *516*, 146155.
- (24) Wang, S.; Desjardins, O. Numerical study of the critical drop size on a thin horizontal fiber: effect of fiber shape and contact angle. *Chem. Eng. Sci.* **2018**, *187*, 127–133.
- (25) Dong, X.; Huang, X.; Liu, J. Modeling and simulation of droplet impact on elastic beams based on sph. *Eur. J. Mech. A Solids* **2019**, *75*, 237–257.
- (26) Zheng, J.; Wang, J.; Yu, Y.; Chen, T. Hydrodynamics of droplet impingement on a thin horizontal wire. *Math. Probl Eng.* **2018**, 2018, 1–10.
- (27) Abishek, S.; Mead-Hunter, R.; King, A. J. C.; Mullins, B. J. Capture and re-entrainment of microdroplets on fibers. *Phys. Rev. E* **2019**, *100* (4), 042803.
- (28) Orkweha, P.; Downing, A.; Lebanoff, A. P.; Zehtabian, S.; Bacanli, S. S.; Turgut, D.; Dickerson, A. K. Ensemble machine learning predicts displacement of cantilevered fibers impacted by falling drops. *J. Fluid Struct.* **2021**, *102*, 103253.
- (29) Lebanoff, A. P.; Dickerson, A. K. Drop impact onto pine needle fibers with non-circular cross section. *Phys. Fluids* **2020**, 32 (9), 092113.
- (30) Derome, D.; Carl, S.; Vontobel, P.; Carmeliet, J. Adsorption and film forming of train of water droplets impacting porous stones. In *Proceedings of the 7th International Building Physics Conference*, 2018; pp 73–78..

- (31) Davis, S. H.; Hocking, L. M. Spreading and imbibition of viscous liquid on a porous base. *Phys. Fluids* **1999**, *11* (1), 48–57.
- (32) Holman, R. K.; Cima, M. J.; Uhland, S. A.; Sachs, E. Spreading and infiltration of inkjet-printed polymer solution droplets on a porous substrate. *J. Colloid Interface Sci.* **2002**, 249 (2), 432–440.
- (33) Gambaryan-Roisman, T. Liquids on porous layers: wetting, imbibition and transport processes. *Curr. Opin. Colloid Interface Sci.* **2014**, *19* (4), 320–335.
- (34) Reis, N. C.; Griffiths, R. F.; Santos, J. M. Parametric study of liquid droplets impinging on porous surfaces. *Appl. Math. Model.* **2008**, 32 (3), 341–361.
- (35) Wijshoff, H. Drop dynamics in the inkjet printing process. *Curr. Opin. Colloid Interface Sci.* **2018**, *36*, 20–27.
- (36) Son, Y.; Kim, C.; Yang, D. H.; Ahn, D. J. Spreading of an inkjet droplet on a solid surface with a controlled contact angle at low weber and Reynolds numbers. *Langmuir* **2008**, 24 (6), 2900–2907.
- (37) Oliver, J. F. Initial stages of inkjet drop impaction, spreading, and wetting on paper. *Tappi J.* **1984**, *67*, 90–94.
- (38) Lee, J. B.; Radu, A. I.; Vontobel, P.; Derome, D.; Carmeliet, J. Absorption of impinging water droplet in porous stones. *J. Colloid Interface Sci.* **2016**, 471, 59–70.
- (39) Griffiths, R. F.; Roberts, I. D. Droplet evaporation from porous surfaces; model validation from field and wind tunnel experiments for sand and concrete. *Atmos. Environ.* **1999**, *33* (21), 3531–3549.
- (40) Lee, J. B.; Derome, D.; Vontobel, P.; Carmelie, J. Absorption of a water droplet impacting on porous media. In *Proceedings of the KNS 2016 Spring Meeting* 1CD-ROM Korea, Republic of. KNS, Engineering, 2016.
- (41) Lee, J. B.; Derome, D.; Carmeliet, J. Drop impact on natural porous stones. *J. Colloid Interface Sci.* **2016**, 469, 147–156.
- (42) Sauret, A.; Boulogne, F.; Cébron, D.; Dressaire, E.; Stone, H. A. Wetting morphologies on an array of fibers of different radii. *Soft Matter* **2015**, *11* (20), 4034–4040.
- (43) Princen, H. M. Capillary phenomena in assemblies of parallel cylinders: II. Capillary rise in systems with more than two cylinders. *J. Colloid Interface Sci.* **1969**, *30* (3), 359–371.
- (44) Duprat, C.; Protiere, S.; Beebe, A. Y.; Stone, H. A. Wetting of flexible fibre arrays. *Nature* **2012**, 482 (7386), 510–513.
- (45) Bico, J.; Roman, B.; Moulin, L.; Boudaoud, A. Elastocapillary coalescence in wet hair. *Nature* **2004**, 432 (7018), 690.
- (46) Yarin, A. L. Drop impact dynamics: splashing, spreading, receding, bouncing. Annu. Rev. Fluid. Mech. 2006, 38 (1), 159–192.
- (47) Moghtadernejad, S.; Lee, C.; Jadidi, M. An introduction of droplet impact dynamics to engineering students. *Fluids* **2020**, 5 (3), 107
- (48) Josserand, C.; Thoroddsen, S. T. Drop impact on a solid surface. *Annu. Rev. Fluid. Mech.* **2016**, *48*, 365–391.
- (49) Bartolo, D.; Josserand, C.; Bonn, D. Retraction dynamics of aqueous drops upon impact on non-wetting surfaces. *J. Fluid Mech.* **2005**, *545*, 329–338.
- (50) Bayer, I. S.; Megaridis, C. M. Contact angle dynamics in droplets impacting on flat surfaces with different wetting characteristics. *J. Fluid Mech.* **2006**, *558*, 415–449.
- (51) Yokoi, K.; Vadillo, D.; Hinch, J.; Hutchings, I. Numerical studies of the influence of the dynamic contact angle on a droplet impacting on a dry surface. *Phys. Fluids* **2009**, *21* (7), 072102.
- (52) Rioboo, R.; Tropea, C.; Marengo, M. Outcomes from a drop impact on solid surfaces. *Atomization Sprays* **2001**, *11* (2), 12.
- (53) Khojasteh, D.; Kazerooni, M.; Salarian, S.; Kamali, R. Droplet impact on superhydrophobic surfaces: a review of recent developments. *J. Ind. Eng. Chem.* **2016**, *42*, 1–14.
- (54) Zhao, P.; Hargrave, G. K.; Versteeg, H. K.; Garner, C. P.; Reid, B. A.; Long, E. J.; Zhao, H. The dynamics of droplet impact on a heated porous surface. *Chem. Eng. Sci.* **2018**, *190*, 232–247.
- (55) Simhadri Rajesh, R.; Naveen, P. T.; Krishnakumar, K.; Kumar Ranjith, S. Dynamics of single droplet impact on cylindrically-curved superheated surfaces. *Exp. Therm. Fluid Sci.* **2019**, *101*, 251–262.

- (56) Tang, C.; Qin, M.; Weng, X.; Zhang, X.; Zhang, P.; Li, J.; Huang, Z. Dynamics of droplet impact on solid surface with different roughness. *Int. J. Multiphase Flow* **2017**, *96*, 56–69.
- (57) Quetzeri-Santiago, M. A.; Castrejón-Pita, A. A.; Rafael Castrejón-Pita, J. The effect of surface roughness on the contact line and splashing dynamics of impacting droplets. *Sci. Rep.* **2019**, 9 (1), 15030.
- (58) Mundo, C. H. R.; Sommerfeld, M.; Tropea, C. Droplet-wall collisions: experimental studies of the deformation and breakup process. *Int. J. Multiphas. Flow* **1995**, *21* (2), 151–173.
- (59) Liang, G.; Guo, Y.; Mu, X.; Shen, S. Experimental investigation of a drop impacting on wetted spheres. *Exp. Therm. Fluid Sci.* **2014**, 55, 150–157.
- (60) Burzynski, D. A.; Bansmer, S. E. Droplet splashing on thin moving films at high weber numbers. *Int. J. Multiphase Flow* **2018**, *101*, 202–211.
- (61) Zen, T.-S.; Chou, F.-C.; Ma, J.-L. Ethanol drop impact on an inclined moving surface. *Int. Commun. Heat Mass Transfer* **2010**, 37 (8), 1025–1030.
- (62) Dickerson, A. K.; Alam, M. D. E.; Buckelew, J.; Boyum, N.; Turgut, D. Predictive modeling of drop impact force on concave targets. *Phys. Fluids* **2022**, *34* (10), 102112.
- (63) Povarov, O. A.; Nazarov, O. I.; Ignat'evskaya, L. A.; Nikol'Skii, A. I. Interaction of drops with boundary layer on rotating surface. *J. Eng. Phys.* **1976**, *31* (6), 1453–1456.
- (64) Yao, S.-C.; Cai, K. Y. The dynamics and leidenfrost temperature of drops impacting on a hot surface at small angles. *Exp. Therm. Fluid Sci.* 1988, 1 (4), 363–371.
- (65) García-Geijo, P.; Quintero, E. S.; Riboux, G.; Gordillo, J. M. Spreading and splashing of drops impacting rough substrates. *J. Fluid Mech.* **2021**, *917*, A50.
- (66) Chebbi, R. Absorption and spreading of a liquid droplet over a thick porous substrate. ACS Omega 2021, 6 (7), 4649–4655.
- (67) Tan, H. Absorption of picoliter droplets by thin porous substrates. *AIChE J.* **2017**, *63* (5), 1690–1703.
- (68) Barui, S.; Ding, H.; Wang, Z.; Zhao, H.; Marathe, S.; Mirihanage, W.; Basu, B.; Derby, B. Probing ink—powder interactions during 3d binder jet printing using time-resolved X-ray imaging. ACS Appl. Mater. Interfaces 2020, 12 (30), 34254—34264.
- (69) Alam, M. E.; Kauffman, J. L.; Dickerson, A. K. Drop ejection from vibrating damped, dampened wings. *Soft Matter* **2020**, *16*, 1931–1940.
- (70) Krsmanovic, M.; Ghosh, R.; Dickerson, A. K. Fur flutter in fluid flow fends off foulers. J. R. Soc. Interface 2023, 20 (209), 20230485.
- (71) Guo, C.; Liu, L.; Sun, J.; Liu, C.; Liu, S. Splashing behavior of impacting droplets on grooved superhydrophobic surfaces. *Phys. Fluids* **2022**, 34 (5), 052105.
- (72) Ojaghlou, N.; Tafreshi, H. V.; Bratko, D.; Luzar, A. Dynamical insights into the mechanism of a droplet detachment from a fiber. *Soft Matter* **2018**, *14*, 8924–8934.
- (73) Gu, W.; Yan, S.; Bai, Z. A study on a droplet impact on a fiber during coalescence-separation: phenomena and models. *Chem. Eng. Sci.* **2020**, *212*, 115337.
- (74) Zhang, G.; Quetzeri-Santiago, M. A.; Stone, C. A.; Botto, L.; Castrejón-Pita, J. R. Droplet impact dynamics on textiles. *Soft Matter* **2018**, *14*, 8182–8190.
- (75) Jordan Bouchard, D. Droplet impact, infiltration, and boiling in pores and porous media. Ph.D. Thesis, University of Toronto, 2021.
- (76) Wang, W.; Du, X.; Vahabi, H.; Zhao, S.; Yin, Y.; Kota, A. K.; Tong, T. Trade-off in membrane distillation with monolithic omniphobic membranes. *Nat. Commun.* **2019**, *10* (1), 3220.
- (77) Wang, W.; Salazar, J.; Vahabi, H.; Joshi-Imre, A.; Voit, W. E.; Kota, A. K. Metamorphic superomniphobic surfaces. *Adv. Mater.* **2017**, 29 (27), 1700295.
- (78) Pritchard, P. J.; Mitchell, J. W. Fox and McDonald's Introduction to Fluid Mechanics; John Wiley & Sons, 2016.
- (79) Wildeman, S.; Visser, C. W.; Sun, C.; Lohse, D. On the spreading of impacting drops. J. Fluid Mech. 2016, 805, 636-655.

- (80) Dickerson, A. K.; Shankles, P. G.; Hu, D. L. Raindrops push and splash flying insects. *Phys. Fluids* **2014**, *26* (2), 027104.
- (81) Pasandideh-Fard, M.; Qiao, Y. M.; Chandra, S.; Mostaghimi, J. Capillary effects during droplet impact on a solid surface. *Phys. Fluids* **1996**, 8 (3), 650–659.
- (82) Clanet, C.; Béguin, C.; Richard, D.; Quéré, D. Maximal deformation of an impacting drop. *J. Fluid Mech.* **2004**, *517*, 199–208.
- (83) Mangelsdorf, S.; Vergou, T.; Sterry, W.; Lademann, J.; Patzelt, A. Comparative study of hair follicle morphology in eight mammalian species and humans. *Skin Res. Technol.* **2014**, *20* (2), 147–154.
- (84) Militzer, K. Haut-und Hautanhangsorgane kleiner Laboratoriumssäugetiere. 1. Vergleichende Morphologie der Haut und der Haare von Maus, Ratte, Hamster, Meerschweinchen und Kaninchen: mit 28 Tabellen; Parey, 1982.
- (85) Meyer, W. Die Haut des Schweines: vergleichende histologische und histochemische Untersuchungen an der Haut von Wildschweinen, Hausschweinen und Kleinschweinen; Schlüter, 1986; Vol. 9.
- (86) Meyer, W.; Schwarz, R.; Neurand, K. The skin of domestic mammals as a model for the human skin, with special reference to the domestic pig1. In *Skin-Drug Application and Evaluation of Environmental Hazards*; Karger Publishers, 1978; Vol. 7; pp 39–52...
- (87) Schwarz, R.; Roux, J. M. W. L.; Neurand, K. Lichtmikroskopische untersuchungen an der haut der katze\*: Verteilung, anordnung morphologie der haare bzw. haarfollikel. *Anat. Histol. Embryol.* **1976**, 5 (4), 325–341.
- (88) Foote, G. B.; Du Toit, P. S. Terminal velocity of raindrops aloft. *J. Appl. Meteorol.* **1969**, *8*, 249–253.
- (89) Sengupta, A.; Behera, J. Comprehensive view on chemistry, manufacturing & applications of lanolin extracted from wool pretreatment. *Am. J. Eng. Res.* **2014**, *3* (7), 33–43.
- (90) Williams, T. D.; Allen, D. D.; Groff, J. M.; Glass, R. L. An analysis of california sea otter (enhydra lutris) pelage and integument. *Mar. Mamm. Sci.* **1992**, *8* (1), 1–18.
- (91) Kaszowski, S.; Rust, C. C.; Shackelford, R. M. Determination of hair density in the mink. *J. Mammal.* **1970**, *51* (1), 27–34.
- (92) Meng, Q.; Wang, Q.; Liu, H.; Jiang, L. A bio-inspired flexible fiber array with an open radial geometry for highly efficient liquid transfer. *NPG Asia Mater.* **2014**, *6* (9), No. e125.
- (93) Lee, K. W.; Liu, B. Y. H. Experimental study of aerosol filtration by fibrous filters. *Aerosol Sci. Technol.* **1982**, *1* (1), 35–46.
- (94) Charles, N. T.; Johnson, D. W. The occurrence and characterization of fouling during membrane evaporative cooling. *J. Membr. Sci.* **2008**, *319* (1–2), 44–53.
- (95) Johnson, D. W.; Yavuzturk, C.; Pruis, J. Analysis of heat and mass transfer phenomena in hollow fiber membranes used for evaporative cooling. *J. Membr. Sci.* **2003**, 227 (1–2), 159–171.